Kinetic Modeling of Solid-State Reaction Synthesis of Single Crystals

Citation

McNamara, Connor P., and Helen M. Chan. *Kinetic Modeling of Solid-State Reaction Synthesis of Single Crystals*. 2024, `https://preserve.lehigh.edu/lehigh-scholarship/graduate-publications-theses-dissertations/theses-dissertations/kinetic-modeling`.

Kinetic Modeling of Solid-State Reaction Synthesis of Single Crystals

by

Connor McNamara

A Dissertation
Presented to the Graduate and Research Committee
of Lehigh University
in Candidacy for the Degree of
Doctor of Philosophy

in
Materials Science and Engineering

Lehigh University
January 2024

DISSERTATION SIGNATURE SHEET

Approved and recommended for acceptance as a dissertation in partial fulfillment of the requirements for the degree of Doctor of Philosophy.

Connor McNamara

Kinetic Modeling of Solid-State Reaction Synthesis of Single Crystals

Defense Date

Dissertation Director

Accepted Date

Committee Members:

Helen Chan

Jeffrey Rickman

Edmund Webb

Hugo Caram

Dedicated to

My late grandfather, the mechanical engineer who encouraged my love of science from day one

Acknowledgments

I want to thank Professors Helen Chan and Jeffrey Rickman for bringing me on to this project. They guided me and helped me become confident in material that I was not that familiar with due to my background in Mechanical Engineering. They saw the potential in me and have given me that push at times I needed to get over that next hurdle.

Our group was small with just me for a while, but it's been fun to see it grow again and even absorb some others. Some of the research wouldn't have been considered if it weren't for the laboratory work of Junyan Zhang. It was fun to have another sneakerhead in the group to discuss latest pickups and our grails.

The biggest thanks go to my parents who have always encouraged me and fostered my love of science. From trips to countless museums to always happily buying educational books that caught my eye. Not to mention putting up with me when the going got rough and I was ready to give up. Also, I'd like to thank my friends here and around the world that I have made through my academic life. I can always reach out to them to discuss nonsense like Marvel movies or which act we think will win Eurovision.

Finally, I want to thank my late grandparents. Their love and support meant the world to me. My Grandmother who always baked something with me when I visited as a child. And my Grandfather who would always do a woodworking project or simple experiment with me, such as making a baking soda volcano or building a robot kit. I always think of them when I look at the work I accomplished or when I bake too many cookies for Christmas.

Contents

List of Figures

Chapter 1

Abstract

Single crystal materials are sought after for their uniform ordered structure and lack of grain boundaries which imparts unique properties to the materials, including mechanical, optical, and electrical. The conventional methods to grow single crystal materials include growth from melt, growth from solution, and growth from vapor, but recently more research has been done on solid-state growth techniques. Solid-state growth is of interest because it presents a more cost effective method to grow smaller scale single crystal materials. One novel method is the formation of pseudo single crystals of compounds with pseudobrookite crystal structures via solid-state reaction from a duplex grain mixture. The pseudo single crystal can be formed from unseeded or seeded powder mixtures. This a more efficient solid-state method and observed growth regimes of some compounds indicate that the final structure can be tuned via templating the powders.

The potential use of templates to control the final microstructure can be capitalized upon by creating a simulation to aid in predicting the outcome. A variety of modeling techniques have been used to model the kinetics of solid-state reactions, such as the shrinking core model, cellular automata, and Monte Carlo simulation. These three methods all have drawbacks for their application to predicting the microstructure in a solid-state system.

The shrinking core model is limited in its scope due to being based on specific geometry and cellular automata is a robust, but computationally intensive method. Kinetic Monte Carlo is the most common technique used for modeling grain growth, but there have been refinements to this model over time. One notable iteration is the Gillespie algorithm, or stochastic simulation algorithm, developed by Daniel T. Gillespie. This was developed for the stochastic solution to coupled chemical reactions, and has been widely used in chemical and biological modeling.

Further refinement of the Gillespie algorithm produced τ-leaping, which speeds up the relatively slow method by incrementing simulation time by a variable τ. This method has not been previously applied to a solid-state system and showed promise that it would be an efficient method that gave control over the starting structures and was not as computationally intensive as previous methods. As such initial testing was focused on ensuring that the model was able to accurately simulate the reaction-diffusion process $A + B \rightarrow C$. A single interface case was simulated where the starting geometry consisted of two regions consisting of purely A and B. The simulation results were evaluated based on the work of Gálfi and Rácz who determined the local rate of production, $R\left(z, t\right)$ of C as a function of z and t at late times. The calculated concentration of C at the interface at late times aligns with the results of the simulation results. Similar agreement for the early time were achieved based on the work of Taitelbaum *et al.*.

The microstructure was expanded to a checkerboard pattern to explore the effects of certain variables in the system. This included diffusivity rates, product stoichiometry, and different diffusivity rates for the A and B atoms. The results give insight into how one can tune the system, such as speeding up or slowing down the product growth and controlling the location of the product phase.

Further geometry was tested by setting the initial microstructure to a top seeded model with alternating vertical strips of A and B atoms. Additionally, this model focused on the condition that the product phase can only grow adjacent to existing product. The time-dependence of the propagating reaction in terms of reactant interdiffusion was studied. Mathematically it was determined that $C_C \propto t^{5/2}$. The proportionality was found in the simulation data plot of the concentration of C vs scaled time. The model was determined to be a good representation of the physical system. Additionally, insight was gained into how the growth rate of the system changes with time.

The microstructure was adjusted further for the final series of simulations which added grain boundaries between the solid A and B regions. This was influenced by discontinuous dissolution reactions in which a migrating front tracks the evolution of a system from a two-phase structure to a single-phase structure. These grain boundaries allowed for a faster diffusion rate when compared to the bulk. The system was run with two initial settings for the grain boundary: with no atoms and with atoms. For the case of no atoms, the relative concentration of C increased approximately as t^3, which was the results of the mathematical analysis. This setting resulted in a lower product production at the seed when compared to the full channel.

Chapter 2

Background

2.1 Single Crystal Processing

Single crystal materials have a crystal structure that is continuous with no grain boundaries and as such are sought after for their uniform ordered structure. One common use is single-crystal silicon in the production of semiconductors. The material has an absence of grain boundaries which would otherwise disrupt electron flow and in turn the overall performance of the component. Another example are the nickel-base superalloys that can be cast as single crystal aircraft turbine blades [11]. The mechanical properties of the blades, such as creep strength and fracture resistance, are improved when compared to equiaxed or directionally solidified blades due to the removal of the grain boundaries.

The conventional methods for producing single crystal materials include: growth from melt, growth from solution, and growth from vapor. The most common of those techniques is growth from melt, where a single crystal is solidified from the melted material [12, 13]. One method of this growth is the Czochralski (CZ) method, predominantly used in the creation of large silicon crystals for wafer processing [1]. In this method a seed crystal is dipped into a melt and slowly removed vertically. The liquid material crystallizes at the seed as it is withdrawn. A schematic of this method is shown in Figure 2.1. The method results in high quality crystals, is relatively quick, and can produce very large crystals. For example, a CZ method grown silicon crystal has a growth rate of around 1 mm/min [14]. A downside to the CZ method is that it can be prohibitively expensive [15].

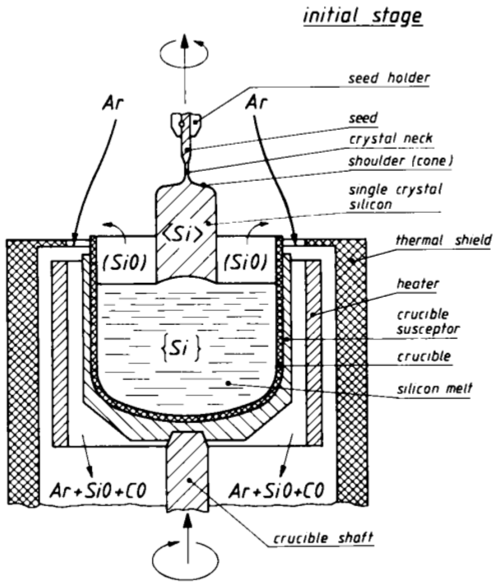

Fig. 2.1. Schematic of Czochralski single crystal growth [1]

Solution growth methods are another category of method that form a solid single crystal from a liquid. In a solution growth method, the material to be crystallized is dissolved in a solvent and the crystal is formed by cooling the solution. A common technique used for forming single crystals of ceramics is flux growth, where the compound is dissolved in a suitable flux. Figure 2.2 shows a schematic of a flux growth furnace. Some of the common fluxes are KF, PbO, and PbF_2 [15, 16]. Flux-growth can be used to grow a wider array or materials than melt as it mainly depends on the existence of an appropriate high temperature solvent [2]. The method is not often used to create the single crystal materials that are intrinsically associated with the CZ method, such as Si, due to some of the limitations of the method. As an example, one may produce Si crystals via Al flux growth, but the overall size of the crystal be be limited by the size of the crucible and it will not grow as quickly as the crystal produced by melt [17]. A more practical application of this method has been its use in the production of piezoelectric single crystals such as PMN-PT and PZN-PT [18]. In addition to the disadvantages mentioned above, the flux may enter the crystal as an impurity.

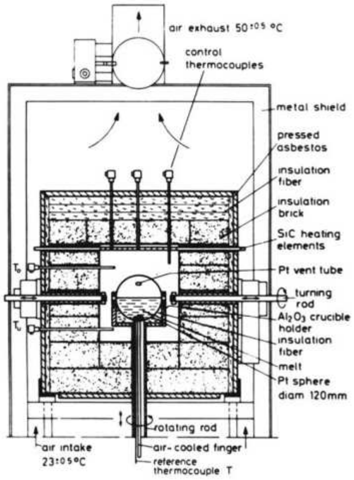

Fig. 2.2. Schematic of a flux growth furnace [2]

Vapor growth is generally used for production of thin single crystal films. This is an umbrella category of methods that all rely on the solidification of a material from the vapor phase and subsequent growth. In all of the techniques, the starting material is located in a distinct source region that is separated from the deposition region which contains a substrate. A thermal field is applied to the system and the now gaseous species are under a potential gradient. The gradient drives the motion from the source to the deposition region [3, 19]. A diagram of the common methods is shown in Figure 2.3. In one method, physical vapor transport (PVT), the solid/vapor transitions occur via sublimation. PVT requires the material have a high sublimation pressure, or else the growth rate will be insufficient due to low vapor density. If the vapor pressure of the material is too low for PVT, chemical vapor transport (CVT) may be utilized [12, 16, 19]. CVT utilizes a gas that reacts with the source material. The source materials is then transported in this new gaseous form to the deposition region where it will react with the substrate and form the solid layer. Vapor growth results in a higher quality crystal when compared to the other techniques, but its size is limited by the equipment. PVT has been used for production of single crystals of CdS, ZnS, and other II-VI compounds [20]. Seeded CVT is often used in the production of materials for photovoltaic applications [21].

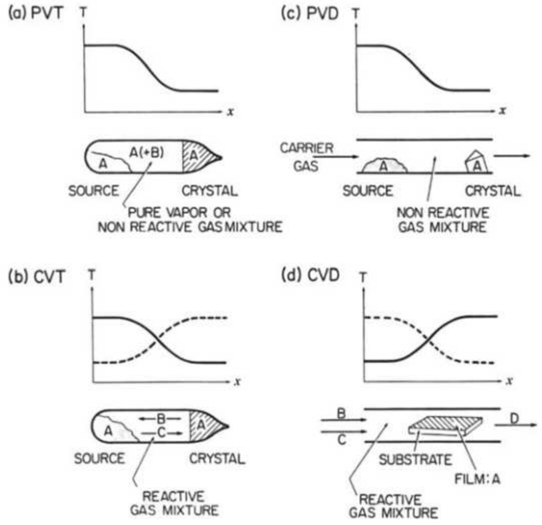

Fig. 2.3. Common vapor growth techniques with the corresponding temperature profiles. a.) Physical vapor transport b.) Chemical vapor transport c.) Physical vapor deposition d.) Chemical vapor deposition [3]

Solid-state growth techniques have also been employed for single crystal growth, but these methods have been not widely used. Recently a novel approach to single crystal growth via solid state reactions of polycrystalline materials has been developed.

2.2 Solid-State Growth of Single Crystals

Solid-state growth techniques can be used for single crystal growth, but these techniques have not been as widely utilized as vapor and melt methods. The atomic diffusion at standard production temperatures is usually slow, which leads to the faster processes being favored. The techniques of solid state growth, including annealing and sintering, were and still are widely used in materials processing. These were not though to be reliable ways to produce large scale pure single crystals. As such, solid-state growth was not widely considered for single crystal processing when more efficient processes exist.

The research of single crystal growth via solid-state reactions was initially limited to metals [22]. This work expanded into the production of single crystal oxide materials. The method focuses on the solid-state conversion of polycrystals into single crystals. This is accomplished via abnormal grain growth in polycrystals. This is a growth phenomenon in where select grains grow at the expense of surrounding normal grains [4]. This is shown in Figure 2.4.

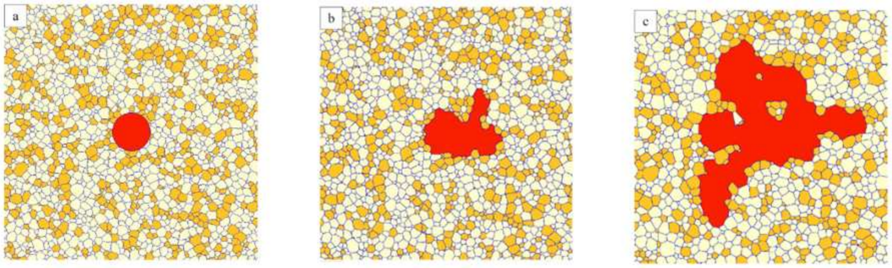

Fig. 2.4. A model of abnormal grain growth [4]

This method was successfully applied to the production of piezoelectric ceramics [18, 23]. With this more modern research into solid-state single crystal production, a method was been found to be more cost effective than some of the ones used previously.

Abnormal grain growth was iterated upon with the addition of a seed crystal into the polycrystal body or on top of it [22, 24]. The growth of the polycrystal must be suppressed while the seed is allowed to grow unhindered. The method is not always viable due to the difficulty of controlling the microstructure of the polycrystal. Another method for controlling the grains in solid state growth is templated grain growth (TGG). In this method, a powder compact that includes a template with shape anisotropy is sintered. The template can be made of the same material as the matrix or it can be a different one (reactive grain growth) [24].

An example of this seeded growth is the production of single crystals of $Pb(Mg_{1/3}Nb_{2/3})O_3$-35 mol% $PbTiO_3$ from polycrystalline precursors [25]. This seeding method relies on the boundary migrating through the polycrystal under the influence of grain boundary curvature. The method was investigated as a more economical method of fabricating single-crystal relaxor-based ferroelectric materials with complex shapes and proven to be feasible. Further studies focused on the factors that influence and control the growth in the system [5, 26, 27]. This includes temporary increase in growth rates due to boundary wetting and the effects of porosity. An example of the growth of the single crystal is shown in Figure 2.5.

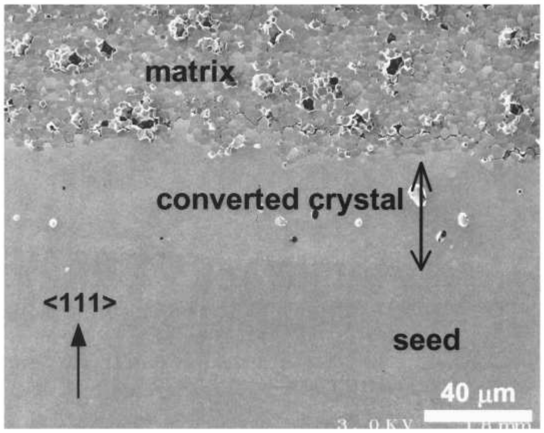

Fig. 2.5. SEM image of the single-crystal/matric boundary region in 1% PbO specimen after 1150°/10 h anneal [5]

The latest development has been the formation of pseudo single crystals of compounds with pseudobrookite crystal structures via solid-state reaction from a duplex grain mixture [6, 28]. The pseudobrookite group exhibit an orthorombic crystal structure (Bbmm) and have a general formula of X_2YO_5 [29,30]. One such compound is $CoTi_2O_5$, which exists as a single crystal line compound from the solid state reaction of $CoTiO_3$ and TiO_2. Figure 2.6 shows the partial phase diagram of the CoO-TiO_2 system where the line compound exists. This reaction does not require seeding or melting as has been previously used in solid state reactions. Work from Anderson et al. [6] investigated and confirmed that $CoTi_2O_5$ is entropy stabilized just as other investigations into pseudobrookite compounds had found [31].

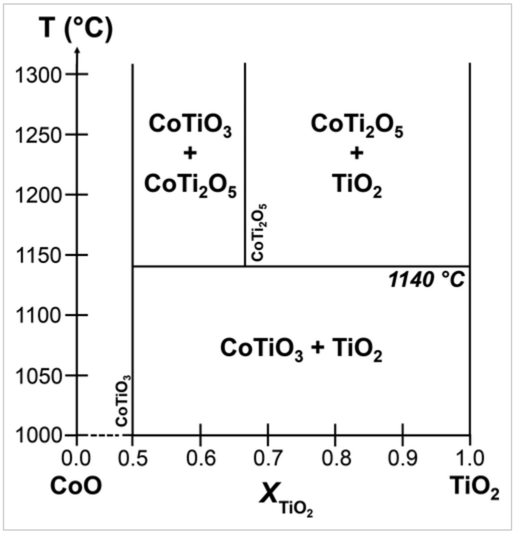

Fig. 2.6. A phase diagram showing the line compound $CoTi_2O_5$ [6]

This pseudo single crystal compound can be formed from unseeded or seeded mixtures of $CoTiO_3$ and TiO_2 powder. The growth of this compound involves two regimes. The first is rapid and occurs preferentially along $CoTiO_3$/TiO_2 diphasic boundaries. The second occurs slowly and involves the diffusion through the $CoTi_2O_5$ lattice [6]. The initial duplex structure will dictate the transformation speed and the degree of subgrain misrepresentation. This novel method is able to convert a two phase mixture into a pseudo single crystal. The mechanics of this transformation are not fully understood and are being investigated further. From the studies that have been done it is potentially a promising new approach for production of single crystals of other pseudobrookite compounds such as $MgTi_2O_5$ and Al_2TiO_5. Also of note in this method, the second growth regime indicates that one can tune the final structure via templating the two powders. The ability to tune the system warrants further study.

2.3 Diffusion Processes

Diffusion is material transport via random atomic motion. Bulk diffusion in a polycrystalline materials, be it interdiffusion or self-diffusion, requires an empty adjacent lattice site as well as sufficient energy for the atom to break its current bonds and deform the lattice. The rate of atomic diffusion for interdiffusion is dependent on relative size of the atoms of the different species. Atoms may also diffuse via interstitial diffusion, in which the atoms diffuse to interstitial sites between the atoms on the lattice. Interstitial diffusion is generally faster than vacancy diffusion due to a lower bond energy between the atoms, but it is still dependent on the relative size of the atoms. Another general method of diffusion in such a material is short-circuit diffusion, or diffusion along defects. These cases include surfaces, grain boundaries, and dislocations. The overall energy needed for diffusion to occur along these pathways is lower as the atoms do not need to deform the lattice.

The rate of mass transfer in a system is dependent on the diffusion coefficient and the concentration gradient. This is expressed as a diffusion flux (J). For a steady state diffusion, the common solution is Fick's first law

$$J = -D\frac{dC}{dx} \tag{2.1}$$

where D is the diffusion coefficient, C the concentration, and x the position in a single direction. D is dependent on the activation energy and the temperature of the system. This can be determined by the Arrhenius equation

$$D = D_0 \exp(-\frac{Q_d}{RT}) \tag{2.2}$$

In this equation, D_0 is a temperature-independent pre-exponential, Q_d is the activation energy, R is the gas constant, and T is the absolute temperature. As can be seen in equation

2.2, the diffusion rate increases with increasing temperature. This is due to the increased energy in the system including the kinetic energy of the atoms allowing for them to overcome the energy barrier associated with moving to a new position. These equations are the basis for stochastic models of steady state atomic diffusion. Similarly, Fick's second law, equation 2.3, is the basis for stochastic models with a concentration that changes over time.

$$\frac{\partial C}{\partial t} = D\frac{\partial^2 C}{\partial x^2} \tag{2.3}$$

With dynamical simulation, the diffusion coefficient can be represented by the sum of the trajectories that contribute to the process [32]. The equation is as follows

$$D_{xx} = \sum_{\alpha} n_\alpha r_{x\alpha}^2 \Gamma_\alpha f_{x\alpha} \tag{2.4}$$

In this equation, D_{xx} is the diffusion coefficient in the x direction, n_α is the geometrical probability of a jump of type α, $r_{x\alpha}$ is the projection of that jump on the x axis, Γ_α is the hopping rate, and $f_{x\alpha}$ is the partial correlation function [32]. This relies on local grouping of potential jump sites for atoms. A variation of this expression can be found in the chemical master equation.

2.4 Master Equation

The chemical master equation (CME) is a stochastic version of the chemical kinetic equation based on the law of mass action [33]. This was developed for liquid or gas phase systems, but it can be applied to solid-state systems. Additionally, variants of the CME are utilized in biological and population modeling. The early work on the CME began in the sixties and the modem version was developed in the nineties [34, 35].

The basis for the CME is the probability of reactants, in a fully mixed system, to react in the next infinitesimal time interval. The probability of a reaction, known as the propensity function, is

$$a_j(x) = c_j x_1 x_2 \tag{2.5}$$

The propensity function, a_j, is based on a reaction constant, c_j, over a time period dt where there are x_i atoms of each species S_j [36]. This propensity function is determined by the order of the reaction and Equation 2.5 is for a second order reaction. As one may note, this is a probabilistic version of the equation for a second order reaction rate.

$$R = k[A][B] \tag{2.6}$$

Where R is the reaction rate, k is a reaction rate constant, and $[A]$ and $[B]$ are the concentrations of species A and B respectively. This is only for a reaction system, but the equation has been expanded for reaction-diffusion systems.

The reaction-diffusion master equation (RDME) is a variation on the CME that includes diffusion events in an inhomogeneous system. Similarly to how the CME is a variation of a reaction rate equation, the diffusion portion of the RDME can be viewed as an extension of Equation 2.1. The diffusion events are described by the diffusion propensity function,

$$a_i(x) = d_i x_i \tag{2.7}$$

In this equation, d_i is the diffusion constant of species S_i and x_i is the number of S_i atoms [37]. Together, Equations 2.5 and 2.7 are the key features of the RDME. This equation is used to solve kinetics problems via stochastic modeling.

2.5 Reaction Diffusion Models

Modeling is a powerful technique that can be used to acquire insight into complex systems. A model allows for tests that might not be feasible in a laboratory due to the cost, time investment, or lack of instruments. This work informs the laboratory work and can make that work more efficient. As such, solid state reactions have been being modeled with a variety of techniques.

One of the earlier modeling techniques used to model the kinetics of solid state reactions has traditionally been based on the shrinking core model [38]. In this model, the reactant phases shrink as they react to form the product phase which in turn forms a barrier between the reactant phases. The shape of the reactant is a variable in the model. An example of these cores is show in Figure 2.7, where the core is a sphere. Models using extensions of the shrinking core and similar approaches are based on specific geometry [39, 40] and thus limited in their scope.

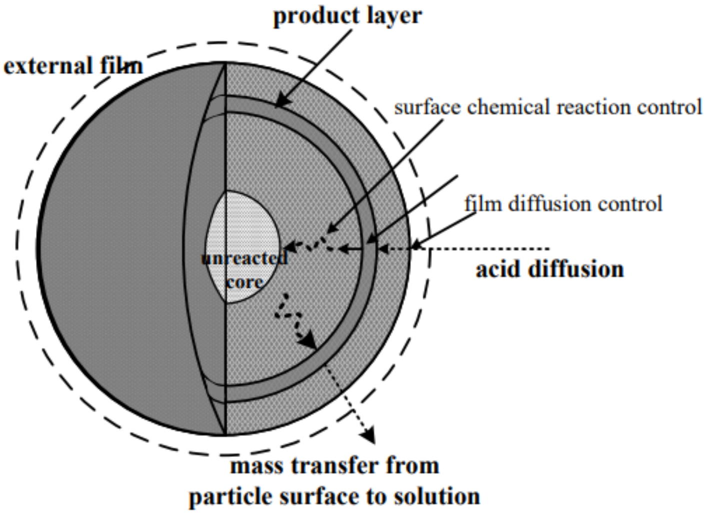

Fig. 2.7. A schematic representation of a shrinking sphere model for aluminum leaching. [7]

A different approach to modeling grain growth kinetics is cellular automata (CA). This method uses a series of cells arranged in a grid that change state as a function of time according to a set of governing localized rules. This has been widely used to model chemical and biological reaction-transport processes [41–44]. Researchers applied this technique to simulating grain growth as well [8]. Han simulated a variety of grain growth scenarios, focusing on grain coarsening and impingement. An example of this study is shown in Figure 2.8.

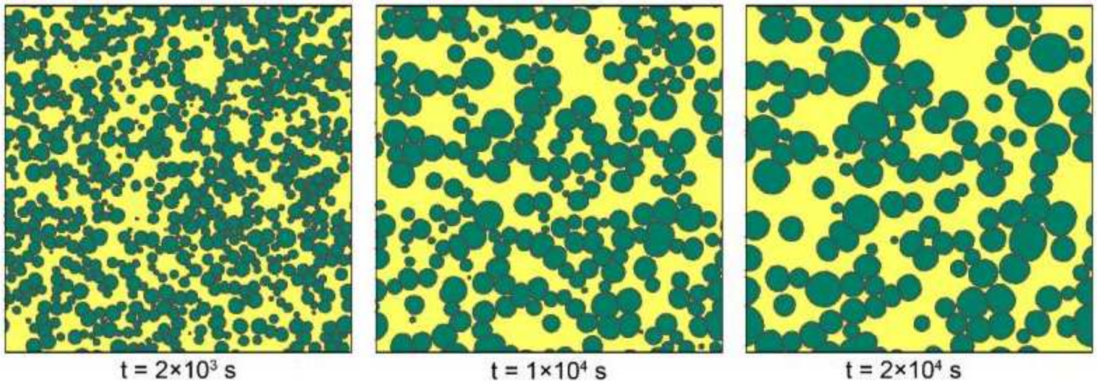

Fig. 2.8. Microstructure evolution over time produced via a cellular automata simulation method. [8]

The earlier modeling techniques were often more qualitatively accurate than quantitatively. As discussed in the work of Weimar and Boon [45], the earlier models for reaction diffusion systems relied on qualitative information about the system and used CA instead of the partial differential equations that governed the system. Weimar and Boon constructed a CA that modeled reaction diffusion systems quantitatively. The method relied on discretization of the variables into small integers and lookup tables as opposed to evaluation of nonlinear functions. This method proved to be more efficient than solving the system with finite difference methods. The method employs some techniques, such as small time discretization, that are used in more modern complex models, but it was held back by computational power for the time.

The CA model is still being refined and improved. One such improvement came from Raghavan and Sahay [9]. Their work improved the grain growth modeling capabilities of CA by allowing fractions of cells to be used for the growth which gives a more continuous snapshot of the grain boundary. The results of which, Figure 2.9, conform to experiments with thin films of succinonitrile. This is a very powerful method that directly maps rules to each cell in the system. With the current state of computing power, a CA model can be run with parallel processing and is very efficient. A downside is that due to needing explicit rules for the transformation in a system it is not as applicable to new systems that are still being examined.

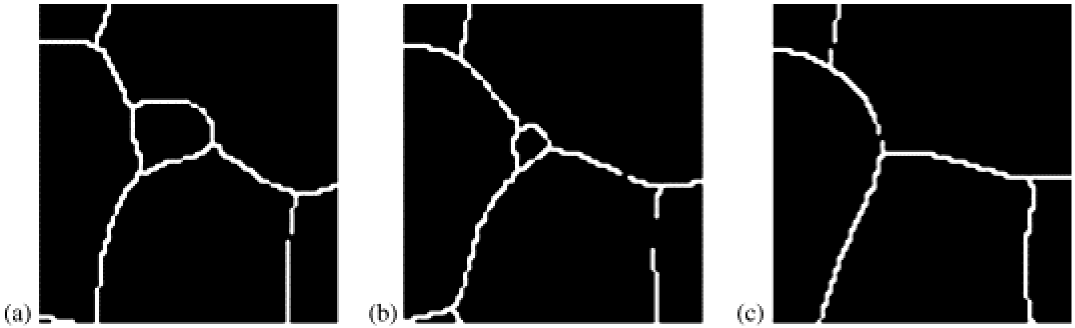

Fig. 2.9. Results of the CA model being applied to the shrinking of a three-sided grain boundary. [9]

Monte Carlo simulation is another modeling approach and is currently the most common technique for modeling grain growth [46]. This method was applied to crystal growth modeling of a solid-on-solid model [47]. In the work of Jiang and Ebner, the results of the dynamical Monte Carlo simulation were compared and related to the Wilson-Frenkel growth rate, in which the activation energy for solidification is equated to the energy barrier for diffusion. They were able to relate the simulation time and physical time for the system by using the simulated and calculated growth rates. This work was compared to equations, but other settings were explored to be able to compare with physical experiments. This work focused on the growth rate in the system, but others have extended this to examine the grain and pore density in a system.

A kinetic Monte Carlo approach was applied to the simulation of grain growth and associated processes during solid state sintering by Braginsky, Tikare, and Olevsky [10]. In this work, their model focused on incorporating densification due to sintering, specifically vacancy migration from pores to grain boundaries and vacancy annihilation. An example of this work is shown in Figure 2.10. The model was novel for being able to realistically simulate this type of microstructural evolution, but it was limited in its ability to properly simulate defect growth. This level of modeling was not previously possible due to the limitations of computing power. Now researchers can utilize more advanced techniques and models with larger more complex microstructures.

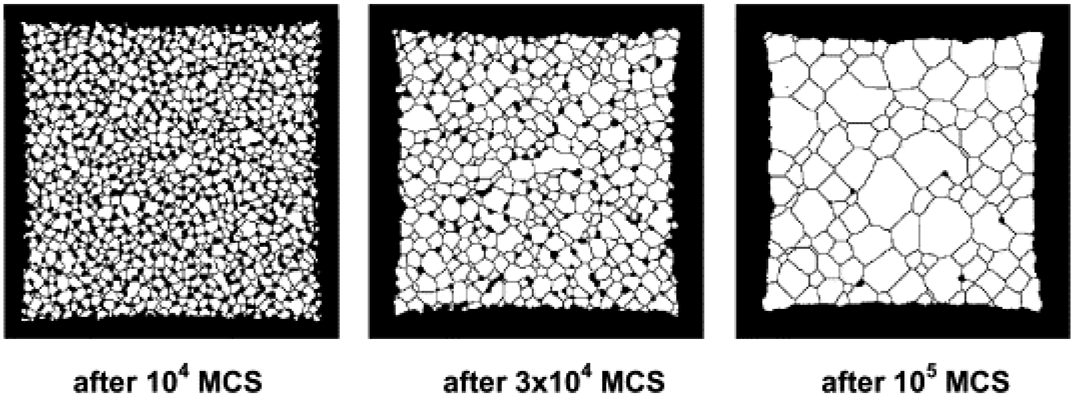

Fig. 2.10. Microstructure evolution after set amounts of Monte Carlo steps (MCS) for a randomly packed non-uniform powder. [10]

2.6 Stochastic Modeling

A stochastic model is a mathematical model in which multiple solutions of governing equations are determined according to a probability curve [48]. Conversely, a deterministic model is one in which a single outcome is predicted from the given criteria. As the deterministic model always returns the same output with set inputs, it limits its use when modeling systems with uncertainty in the variables and events. The ability to use random variables in the model has been appealing to chemical kinetics modeling as well as biological modeling [49, 50]. The stochastic modeling techniques have been iterated upon and refined as computing power has increased.

One of the most used methods of stochastic modeling is the Monte Carlo method. A Monte Carlo simulation relies on repeated random sampling of probability density functions. As this relies on random numbers, the advent of more accessible computing has accelerated the use of this type of model. The Monte Carlo method has been refined and iterated upon by mathematicians and researchers. One such variation is the Gillespie algorithm.

The Gillespie algorithm, also known as the stochastic simulation algorithm, utilizes Monte Carlo simulation to simulate the evolution of a chemical system over time. This algorithm came to prominence with the work of Daniel T. Gillespie developing a stochastic solution to coupled chemical reactions [51, 52]. The general flow for the stochastic simulation algorithm is presented below.

Stochastic Simulation Algorithm

1. Initialize the system
2. Generate random numbers
3. Calculate the time step
4. Evaluate the master equation with the time step and random numbers
5. Repeat from step 2 until the set time has elapsed

This method can be time intensive as it is relatively slow. A modified Gillespie method called τ-leaping speeds up the process by incrementing time in the simulation by a variable τ [53–55]. The method also differs from the standard Gillespie method in that the random variables are generated from a Poisson distribution. The τ-leaping method algorithm is described below.

Tau-leaping Algorithm

1. Initialize the system

2. Generate Poisson random numbers
3. Evaluate the master equation using the random numbers
4. Increment time by τ
5. Repeat from step 2 until the set time has elapsed

2.7 Methodology

The τ-leaping algorithm described above was extended to model the kinetics of reactive phase formation comprising multiple diffusion and reaction events that initiate at interphase boundaries. The features of this model are the two-dimensional array that represents a simulation microstructure and the modified algorithm.

The representational array used in the model is a two-dimensional $L_1 \times L_2$ spatially periodic computational cell partitioned into K pixels, each pixel having an edge length h. The starting duplex microstructure consisting of pure phases α and β comprising multiple pixels is superimposed on this computational lattice such that pixels of α and β initially contain N A or B “atoms”, respectively. When these atoms are in proximity they react to form C according to $A + B \rightarrow C$, where the stoichiometry of $C = A_m B_n$ and m and n are integers. This microstructure is tailored to the needs of the simulation by varying the location and concentration of the A and B atoms. Additionally, a “seed” of product C atoms can be included in the system for models simulating epitaxial growth. The microstructure setup is only one component of the model initialization.

While discussing methodology, the chemical species A, B, and C are denoted as $1 - 3$ respectively. The state of the system at time t can be described as a state matrix $\bar{X}(t)$ whose components $X_{ik}(t)$ are the number of atoms of species i ($i = 1, 2, 3$) in pixel k ($k = 1, 2, \cdots, K$) at time t. Three stochastic processes are considered, the chemical reaction and the diffusion of A and B atoms. (C atoms are taken to be immobile.) The rates associated with these processes include a reaction probability density $a_k\left(X_{ik}\left(t\right)\right)$, the probability per unit time that a reaction occurs in pixel k when the state of that pixel is given by $X_{ik}\left(t\right)$ at time t, and diffusion probability densities $a_{ik\vec{e}}^{d}\left(X_{ik}\left(t\right)\right)$, the probability per unit time that a diffusive transition occurs of species i from pixel k to a nearest-neighbor pixel in direction $\vec{e}$ when the state of the starting pixel is given by $X_{ik}\left(t\right)$ at time t. (For the geometry considered here $\vec{e} \in \mathcal{E}$, where $\mathcal{E}$ is the set of four nearest-neighbor directions for a square lattice.)

Diffusion and reaction events are taken as occurring at random during τ as described by Poisson processes with mean event numbers determined from the associated probability densities, respectively. For the simulation of reaction events in a given pixel, a random number is drawn from a Poisson distribution. Alternately, for diffusion events for species i ($i = 1, 2$), the random number is drawn from a truncated Poisson distribution that is constrained to produce a result between zero and $X_{ik}\left(t\right)$. It is assumed that reactions are described by second-order kinetics for pixel k such that the corresponding rate is proportional to $X_{1k}\left(t\right)X_{2k}\left(t\right)$. The numbers drawn in this way dictate the corresponding number of subsequent transitions. Two reaction scenarios were considered in this model. The first scenario, referred to as the non-plating case, has the rate of C production independent of the location of other C atoms in the system. The second case (plating) differs by having the rate of C production be catalyzed by the presence of C atoms in neighboring pixels.

The simulation procedure is as follows. The system is initialized at $t = 0$ by setting the diffusion and reaction rates as well as the starting duplex microstructure. For each iteration, the algorithm increases time by a step of τ and a reaction or diffusion event is chosen with equal probability for each pixel. A random number is drawn from one of the previously mentioned distributions having a mean of either $a_k\left(X_{ik}\left(t\right)\right)\tau$ or $a_{ik\vec{e}}^{d}\left(X_{ik}\left(t\right)\right)\tau$, the former corresponding to the number of reaction events and the latter the number of diffusion events. These numbers dictate the necessary changes in the occupancy matrix components $X_{ik}(t)$ for both the pixel k and nearest-neighbor pixels. Note, reaction events are based on the number of reacting atoms available locally in addition to the reaction rate. In the event of null occupancy the algorithm records no event and moves to the next step. When the local occupancy is lower than the reaction event value, the reaction is scaled to meet the value of the limiting atom species in the cell. The procedure is repeated for $\mathcal{N}$ iterations with the simulation time advancing by τ for each iteration until the total amount of time T is achieved. To draw statistically meaningful conclusions, the results are averaged over $\mathcal{N}$ independent runs (or R runs).

Solid-State Kinetics tau-leaping algorithm

1. Initialize the time $t = 0$ and the state matrix $\bar{X}(t_0)$
2. Random choice to determine if reaction or diffusion events will occur first
3. For the event chosen, a pixel k is chosen randomly
4. A random number is drawn from $a_k(X_{ik}(t))\tau$ or $a^d_{ik\vec{e}}(X_{ik}(t))\tau$ depending on the event
5. The occupancy matrix $X_{ik}(t)$ for the pixel k and potentially nearest-neighbors are updated accordingly
6. Return to step 3 until K events have been completed
7. Steps 3 through 5 are repeated for the event that was not picked in step 2
8. Update t to $t + \tau$
9. Return to step 2 until $t = T$
10. Update r to $r + 1$ and save the state matrix $\bar{X}_r(T)$

11. Return to step 1 until $r = R$
12. Average the results

The algorithm allows for a variety of additional conditions for the system. For example, the simulation of epitaxial growth was mentioned previously. In this condition, the algorithm checks for the presence of C atoms in neighboring pixels before the reaction event is calculated. Additionally, the algorithm allows for multiple diffusion rates to be used. The simulation can apply these rates to A and B atom motion or it can be applied to different areas of the microstructure.

Chapter 3

Statement of Purpose

Solid-state reactions are utilized for the processing of complex materials, and recent research has demonstrated the efficacy of using this technique to produce a pseudo single crystal in systems that have entropy-stabilized line compounds. This reaction initiates from a compositionally inhomogeneous patterned structure. The method is novel and there has been no work done on an associated model. The objective of this research is to create a 2D stochastic model of a solid-state second-order reaction. This model includes a starting microstructure that is chosen by the user. Previous kinetic models of solid-state reactions utilizing methods such as dynamical Monte Carlo do not have the ability to designate starting microstructures. This model utilizes τ-leaping as it is a more efficient stochastic algorithm than the ones traditionally used in materials science and includes tuneable microstructures. A comprehensive kinetic model allows for the prediction of the resultant microstructure produced from the reaction. The work will apply and validate a technique that has not been used on material systems and will additionally further the knowledge of a nascent process for producing single crystal materials.

Chapter 4

Kinetics and Associated Microstructure for Reactive Phase Formation

4.1 Introduction

Solid-state reaction is widely utilized for the processing of complex materials [56–58]. For example, this technique has been used to synthesize a wide variety of ceramic compositions for structural and electronic applications [59–69]. In these applications, there are several geometries that have garnered attention due to their relevance to ceramics processing; these include geometries that promote reactions between thin films and substrates [59–62], and between powder particles of the reactant phases [63–69].

Consider a prototypical second-order reaction in which reactants A and B combine to form the product phase C, as denoted by $A + B \rightarrow C$. Traditionally, the kinetics of solid-state reactions have been analyzed based on a shrinking core model [70]. Because the product phase forms a barrier that physically separates the two reactant phases, the reaction proceeds by solid-state diffusion through C. In most treatments of reaction kinetics, nucleation of the product is usually assumed to occur instantaneously, and hence does not constitute a kinetic barrier. Typically, the experimental data is fit to a particular model, and the results used to infer the rate limiting diffusive species. The models used in this type of approach are typically geometry and microstructure sensitive, and have been reviewed by Khawam and Flanagan [39] and Chandratreya [71]. For an idealized geometry (i.e, linear diffusion and planar interfaces), the kinetics of these types of reactions have been treated quantitatively by Wagner [72] and Schmalzried [73, 74]. Alternatively, cellular automata (CA), whereby lattice sites are populated with atomic species and the system evolves (by diffusion and reaction) according to specified local rules, have been employed to model reaction-transport processes for a broad range of chemical, physical and biological phenomena [42–44, 75].

In general, with regard to solid state synthesis, the focus has been on modeling the kinetics of the reaction. However, the microstructural evolution resulting from a patterned template (e.g., a starting A-B duplex structure) that transforms via solid-state reaction has received little to no attention. It is noted that from an experimental standpoint this type of reaction has rarely been reported. This is in large part because, for most material systems, it is difficult to identify processing conditions that will result in a dense two-phase mixture of A and B, without the concomitant production of C. An interesting exception to this practical difficulty is a special class of complex ceramics that have been described as entropy-stabilized [31]. These systems are line compounds that are thermodynamically stable only above a certain critical temperature, T_c; below this temperature, the corresponding composition falls within a two-phase field. For suitable values of T_c, therefore, it may be possible to process dense two phase mixtures below T_c, and to induce a reaction by subsequent heat treatment at temperatures greater than T_c. One such system is Co-Ti-O, which contains the entropy stabilized composition cobalt dititanate, $CoTi_2O_5$ [31, 76].

Recent work by Anderson *et al.* [6] has revealed that a duplex microstructure of $CoTiO_3$ and TiO_2 grains is obtained by sintering a mixture of CoO and TiO_2 powders at 1150°C.

Following annealing treatments at temperatures in the range 1200-1400^{o}C, the two phases reacted along the bi-phasic boundaries to form $CoTi_2O_5$. Figure 4.1 shows an EBSD map highlighting the relevant phases that is taken from the work of Anderson *et al.* Two $CoTi_2O_5$ growth regimes were considered. It was reported that the first regime is relatively rapid, and is governed by diffusion at interphase boundaries, and involves $CoTi_2O_5$ growth through the $CoTiO_3/TiO_2$ mixture. The second regime occurs more slowly, taking place by diffusion through the $CoTi_2O_5$ lattice, with eventual elimination of isolated $CoTiO_3$ and TiO_2 grains. A notable (and surprising) finding was that characterization by EBSD (electron backscattered diffraction) revealed that the $CoTi_2O_5$ was essentially single crystal. The afore-described process of single crystal generation is novel and has not been reported previously in ceramic systems.

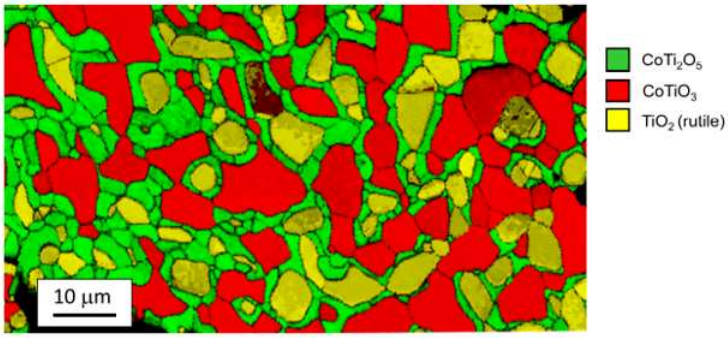

Fig. 4.1. EBSD phase map obtained from polished cross sections of air-quenched powder particles formed from the solid-state reaction of CoO and TiO_2 at 1200^{0}C for 15 minutes. The starting microstructure is a duplex mixture of $CoTiO_3$ and TiO_2 grains [6]. Note the growth of single crystal $CoTi_2O_5$ along the biphasic boundaries

Given the reactions initiated in the complex, starting bi-phasic microstructures described above, it is of interest to determine how the starting structure and the associated reaction kinetics can give rise to a rich variety of product-phase microstructures. Rather than focusing exclusively on ceramic systems, solid-state kinetics in selected templated models will be examined. Thus, the aim of this work is to model the microspotructural evolution of a product phase that is produced via solid-state reaction that initiates on a bi-phasic template. The approach will be to establish first a simulation strategy that will permit the modeling of the reaction-diffusion kinetics with a starting template that results in an evolving product phase. This will be accomplished by adapting an approach developed to simulate reaction-diffusion kinetics in chemical systems. The next step is to consider prototypical templates and investigate in detail the kinetics and morphologies of product microstructure as a function of geometric and kinetic parameters. It is clear that the patterns present in the final microstructure will depend on the spatial arrangement of these reacting phases. Thus, the length scales inherent in the template, together with the energy and time scales that dictate the diffusion and reaction kinetics, conspire to produce a given product microstructure, and it is imperative to understand the roles played by relevant template parameters in dictating this microstructure. By extension, therefore, a knowledge of these scales permits the construction of templates that may be employed to facilitate microstructural design. Viable design strategies based on this work will examined in the Discussion and Conclusions section.

4.2 Results

Two prototypical duplex microstructures are employed here that highlight the role of templating and product-phase stoichiometry in determining the product microstructure resulting from reaction-diffusion kinetics. Figure 4.2a shows the geometry associated with a single interface where initially pure A α and pure B β phases meet, and Fig. 4.2b shows a checkerboard geometry comprising alternating α and β phases. In the latter case, a seed initially consisting of only C atoms is also included. The aim is to understand the impact of the starting microstructure on the spatio-temporal evolution of the product phase, first for $C = A_nB_m$ with $n = m = 1$ and then for other stoichiometries, under a variety of kinetic conditions.

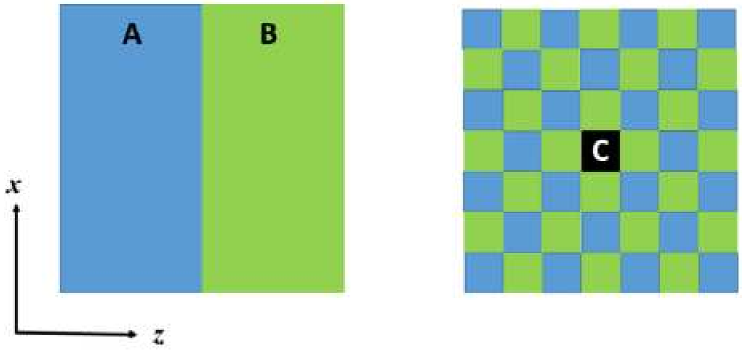

Fig. 4.2. a.) The planar interface geometry where initially pure A α and pure B β phases meet. b.) The checkerboard geometry comprising alternating α and β phases and a pure C seed.

4.2.1 Single Interface

To validate the simulation methodology, we consider the reaction-diffusion processes $A + B \rightarrow C$ that initiates at time $t = 0$ at a single planar interface $z = 0$ in a system with $L = 110$ such that the region $z > 0$ ($z < 0$) consists solely of A (B) atoms and that there are initially no C atoms (see Fig. 4.2a). The aforementioned plating condition is not operative for this test case. We note that this reaction-diffusion scenario was examined quantitatively in a mean-field approximation by Gálfi and Rácz [77] who were able to determine the local rate of production, $R\left(z, t\right)$ of C as a function of z and t at late times, and subsequently by [78] using a cellular automata. The governing equations for the concentrations $C_A\left(z, t\right)$ and $C_B\left(z, t\right)$ of A and B, respectively, are

$$\frac{\partial C_A}{\partial t} = D_A \nabla^2 C_A - kC_A C_B,$$

$$\frac{\partial C_B}{\partial t} = D_B \nabla^2 C_B - kC_A C_B, \tag{4.1}$$

(4.2)

where D_A (D_B) are the diffusivities of the A and B atoms, respectively. For simplicity, we consider here the equal diffusivity case, $D_A = D_B = D$, and impose the initial conditions that $C_A^0 = C_A(z, 0)$ for $z > 0$ and $C_B^0 = C_B(z, 0)$ for $z < 0$. (The case of unequal diffusivities will be considered below.) Gálfi and Rácz find at late times for the geometry outlined above that if $C_A^0 = C_B^0$, then $R(z, t) \sim t^{-2/3}\ F\left[z/t^{1/6}\right]$, where F is a scaling function. Thus, if one focuses on the interface where $z = 0$ and then integrates $R(0, t)$ over time, one finds that $C_C(z = 0, t) \sim t^{1/3}$ at late times.

We first compare the simulation results with those obtained by numerical integration of the coupled, non-linear differential equations given by Eqs. (4.1). These equations can be written in dimensionless form by identifying the fundamental length and time parameters $\ell = \sqrt{D/kC_A^0}$ and $\theta = 1/kC_A^0$, respectively. Figure 4.3 shows a plot of $C_C(z = 0, t)/C_0$, where $C_0 = C_C(z = 0, t = 0)$, as a function of t as obtained from our simulations and via numerical integration for system size $L = 110$ and $D = 5.0$ and $k = 0.05$ for $\mathcal{N} = 30$. As there is no direct link between τ and θ, the τ-leaping time was scaled to produce the best agreement with the numerical integration results. As can be seen from the figure, $C_C(z = 0, t)/C_0 \sim t^{1/3}$ (approximately) at late times, as expected.

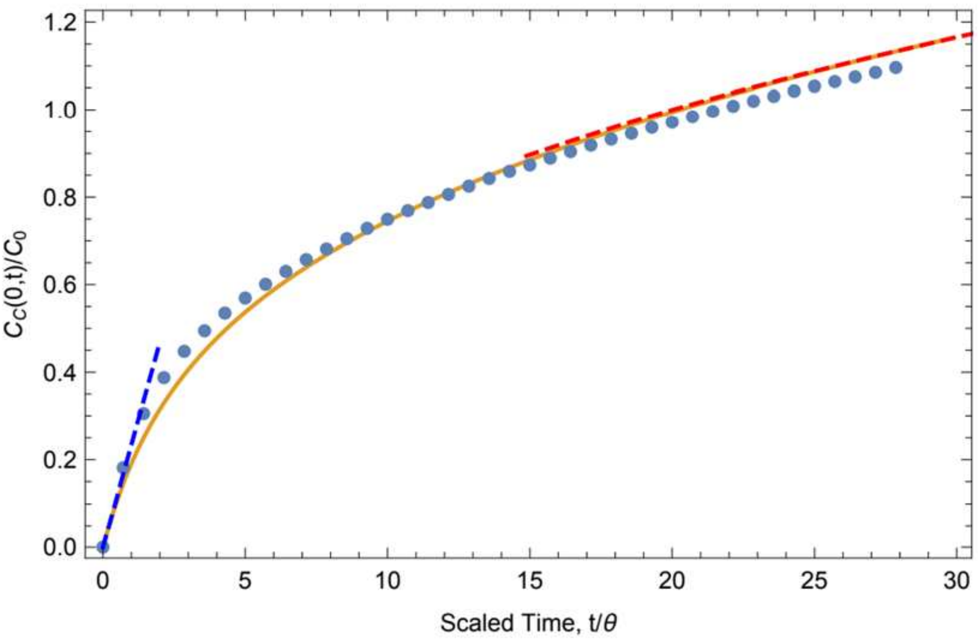

Fig. 4.3. The concentration of C atoms, $C_C\,(z=0,t)$, as a function of reduced time, t/θ, as obtained from our simulations of a single interface between initially pure A and pure B regions. Each pixel initially contains 40 atoms of either type A or B. For these simulations $L=110$ with $D=5.0$ and $k=0.05$ and the results have been averaged over $\mathcal{N}=30$ independent runs. Also shown (solid line) is $C_C\,(z=0,t)$ as obtained by numerical integration of Eqs. (4.1). In addition, at late times the red, dashed curve is a power law fit $\sim t^{0.37}$ and at early times the blue, dashed curve is a linear fit $\sim t/4$. The results were averaged over $\mathcal{N}=30$ independent realizations of this system.

At early times one can determine $C_C\,(z=0,t)$ for diffusion-dominated kinetics (i.e., for $\epsilon := k/D$ small). For this limiting case, Taitelbaum *et al.* [79] applied perturbation theory in ϵ to obtain, to first order in ϵ, the local rate of product-phase formation

$$R\,(z,t) \approx \frac{k}{4}\left[1+\operatorname{erf}\left(\frac{x}{2\sqrt{Dt}}\right)\right]\left[1-\operatorname{erf}\left(\frac{x}{2\sqrt{Dt}}\right)\right]. \tag{4.3}$$

The presence of the error functions in Eq. (4.3) indicates that $R\,(z,t)$ is governed at early times largely by the interdiffusion of A and B atoms for diffusion-dominated kinetics, as expected. One therefore expects that $C_C\,(z=0,t)\sim t/4$ at early times, as can also be seen in Fig. 4.3. It is also of interest to examine the total amount of product that exists at a particular time. For an infinite, continuous system, one expects that the total amount of C produced in the diffusion-dominated kinetics limit is given by

$$C_C^{tot}(t) = \int_{-\infty}^{\infty} dz\, R(z,t) \propto \sqrt{t}. \tag{4.4}$$

4.2.2 Checkered Microstructure

Consider next a $L = 70$ checkerboard microstructure that is subdivided into blocks of pure α and β, each pixel within a block containing 20 atoms of type A or B at $t = 0$, and a central block consisting entirely of 1000 immobile C atoms at $t = 0$ (see Fig. 4.2b). This system evolves according to reaction-diffusion dynamics for different scenarios involving either plating or non-plating conditions. Our focus here will be on the total amount of product that exists at a particular time, namely $C_C^{tot}(t) = \sum_{\{\vec{r}\}} C_C(\vec{r},t)$. The sum here is over all pixels comprising the checkerboard lattice. As we are interested in quantifying the spatio-temporal evolution of the C atoms, we characterize the extent of the product "cloud" at time t by its radius of gyration, $R(t)$. More specifically, by analogy with a spatial distribution of masses, we calculate the gyration tensor from $C_C(\vec{r},t)$ and obtain the squared radius of gyration from the sum of the squares of its (ensemble averaged) eigenvalues, λ_1 and λ_2. [80]. As we consider cases where the kinetics is isotropic, $\lambda_1 - \lambda_2 = 0$.

High- and Low-Diffusivity Cases

We first examine the high-diffusivity (low-ϵ) case for which $\epsilon = 0.01$. The resulting concentration of C atoms, $C_C^{tot}(t)$, and late-time microstructures for the plating and non-plating conditions are summarized in Figs. 4.4 a and c, respectively, and the corresponding rates of change of the amount of C atoms, dC_C^{tot}/dt, are shown in Figs. 4.4 b and d, respectively.

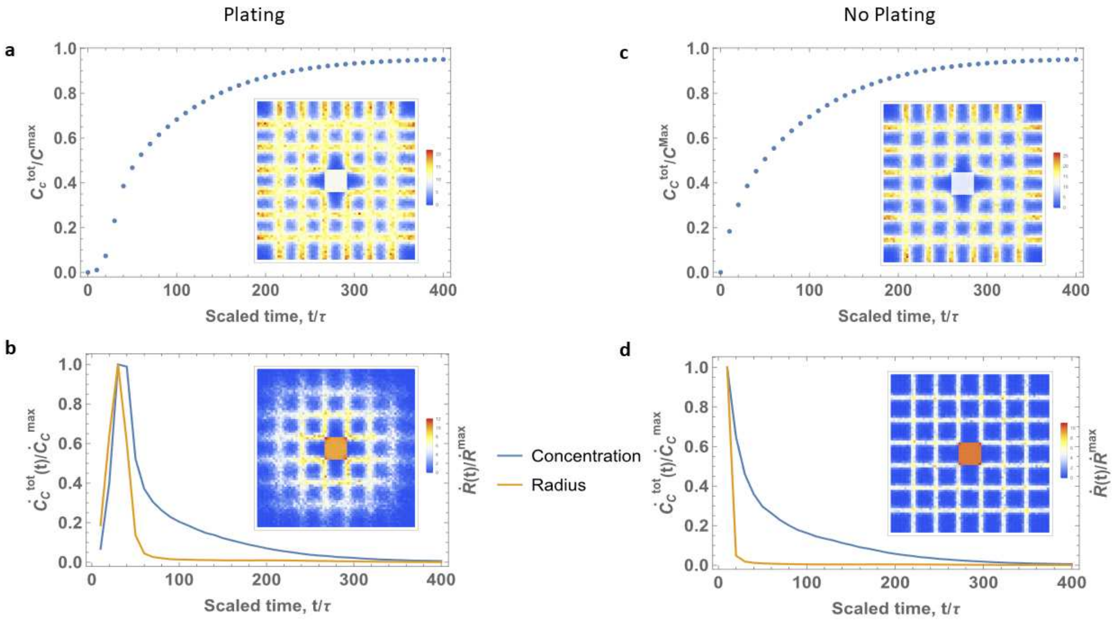

Fig. 4.4. a.) The concentration of C atoms, $C_C^{tot}\left(t\right)$, as a function of reduced time, t/θ, for the plating case and $\epsilon = 0.01$. Also shown is the late-time average microstructure $C_C\left(\vec{r}, t\right)$ (inset). For the microstructural insets, the color range from red to blue indicates a range of C_C from high to low. b.) The rate of change of the amount of C atoms, $\dot{C}_C^{tot}\left(t\right)$ normalized by its maximum value $\dot{C}_C^{max}$, (blue curve) and the time rate of change of the radius of gyration, $\dot{R}\left(t\right)$ normalized by its maximum value $\dot{R}^{max}$, (orange curve) versus t/τ corresponding to (a). Note that the peak production of C corresponds nearly to the maximum extent of C along the phase boundaries, as is evident from the corresponding microstructure (inset) showing the microstructure at peak production. c.) The same as (a), except for the non-plating case. d.) The same as (b), except for the non-plating case. Note that the absence of the plating constraint leads to a rapid propagation of the C atoms along phase boundaries. These results were averaged over $\mathcal{N} = 30$ independent realizations of this system.

A comparison of Figs. 4.4a and 4.4c reveals the different early time behavior of the plating and non-plating cases, respectively. In particular, the behavior of the non-plating case is analogous to that observed for a single interface (see Fig. 4.3) while, for the plating case, $C_C^{tot}\left(t\right)$ is non-linear at early times. In this latter case, the propagation of C at early times can be viewed to a good approximation as a hopping process in which the production of C in a given pixel depends on its presence in neighboring pixels. As can be seen from Fig. 4.4b, the peak rate of production of C corresponds roughly to the peak rate of change of the the radius of gyration, indicating that the enhanced production of C requires the propagation of this product phase along interphase boundaries. By contrast, without the plating constraint, the product forms quickly at all interphase pixels and the location of the seed is essentially irrelevant. Thus, the peak rate of production of C occurs almost immediately after the start of the reaction, as is evident from Fig. 4.4d.

It is also of interest to contrast these results with those of the low-diffusivity case (high-ϵ) for $\epsilon = 0.1$ as shown in Figs. 4.5. First, a comparison of high-diffusivity case summarized in Figs. 4.4 a and c with the corresponding low-diffusivity case presented in the corresponding Figs. 4.5 a and c reveals that the reaction has progressed further in the former case, as expected. Moreover, in the high-diffusivity case, the evolving product microstructure comprises relatively diffuse strips, as opposed to the low-diffusivity case, forming at the original interphase boundaries. Thus, the width of the product phase is determined, at least in part, by ϵ.

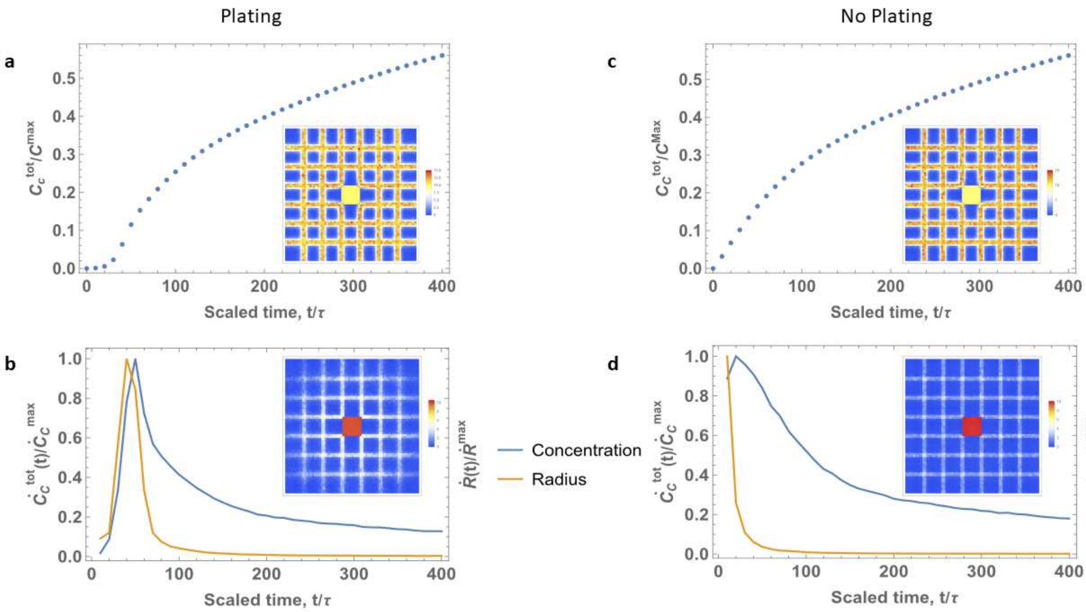

Fig. 4.5. The same as Fig. 4.4, except for the low-diffusivity case for $\epsilon = 0.1$ For the microstructural insets, the color range from red to blue indicates a range of C_C from high to low.

Impact of Product Stoichiometry

We next consider the role of product stoichiometry in dictating product microstructure. It is expected, *a priori*, for $C = A_m B_n$ that reactant location and exhaustion will dictate the morphology and spatial extent of C when $|m - n|$ becomes large. To examine this claim, we compare the kinetics and microstructure for two different products, namely $C = A_2 B_1$ and $C = A_1 B_1$. Figure 4.4a compares $C_C^{tot}(t)$ for these products under plating conditions with $\epsilon = 0.1$.

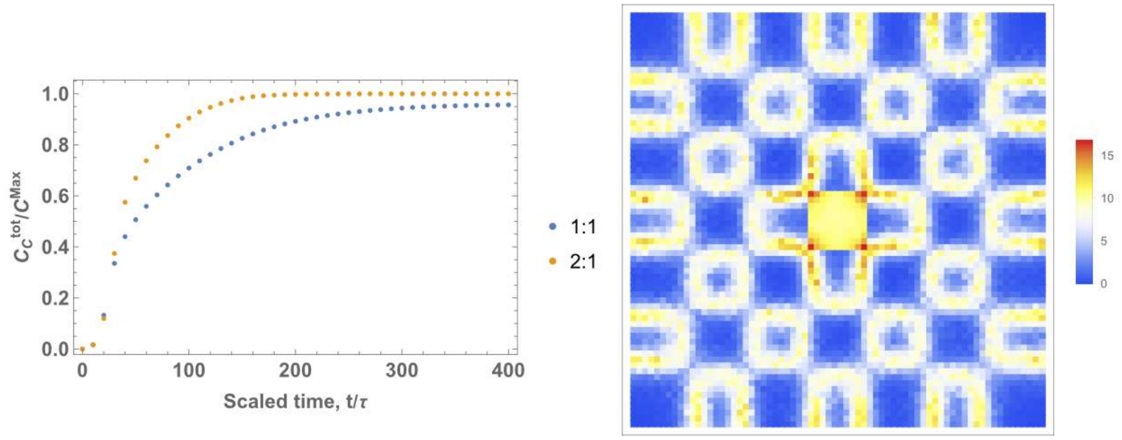

Fig. 4.6. a.) The concentration of C atoms, $C_C^{tot}(t))$, for different stoichiometries as a function of reduced time, t/θ, for the plating case and $\epsilon = 0.1$. The stoichiometric coefficients are $C = A_2B_1$ (orange curve) and $C = A_1B_1$ (blue curve). b.) The corresponding average microstructure at late time. The color range from red to blue indicates a range of C_C from high to low.These results were averaged over $\mathcal{N} = 30$ independent realizations of this system.

As is apparent from Fig. 4.6a, the total amount of $C = A_2B_1$ is less than that of $C = A_1B_1$, as expected since twice as many A atoms are required to produce one C atom. The microstructural implications of stoichiometry are evident from Fig. 4.6b where it can be seen that the final, average product microstructure comprises alternating blocks, with the A-rich blocks containing a higher concentration of C. The product phase is not, however, uniformly distributed within such blocks, with regions poor in C near the block centers resulting from the requirement that the diffusion of B atoms is required for the production of C. Thus, the initial duplex structure may be tuned to induce product microstructural patterns that vary with stoichiometry.

Impact of Diffusivities

We next examine the impact of unequal diffusivities on product-phase kinetics and microstructure. Figure 4.7 shows the time dependence of the normalized concentration for the case where $D_B/D_A = 1$ as compared with the corresponding quantity for $D_B/D_A = 5$ under non-plating conditions. Clearly, an imbalance in diffusivities results in less C production at intermediate times. One can rationalize these results by considering, for simplicity, the production of C at a single A-B interface ($z = 0$, as above) for the extreme case $D_B/D_A >> 1$. For this scenario the A atoms are relatively immobile on the time scale of B diffusion, with the result that $C_A\,(z = 0, t)$ is essentially fixed at early times. Thus, impinging B atoms reacting with a fixed C_A produce a limited number of C atoms at $z = 0$, even at late times. One then infers that, more generally, for $D_B/D_A > 1$, the late-time value for $C_C\,(z = 0, t)$ is less that for the case where $D_B/D_A = 1$.

The corresponding microstructures for both plating and non-plating cases for $D_B/D_A = 5$ are shown in Fig. 4.8. As is evident from the figures, in both the plating and non-plating cases, the distribution of C atoms at late times is inhomogeneous, with larger concentrations in regions where the original duplex structure is B-rich. It follows from these results that both D_B/D_A and $|m - n|$ control the product-phase microstructure.

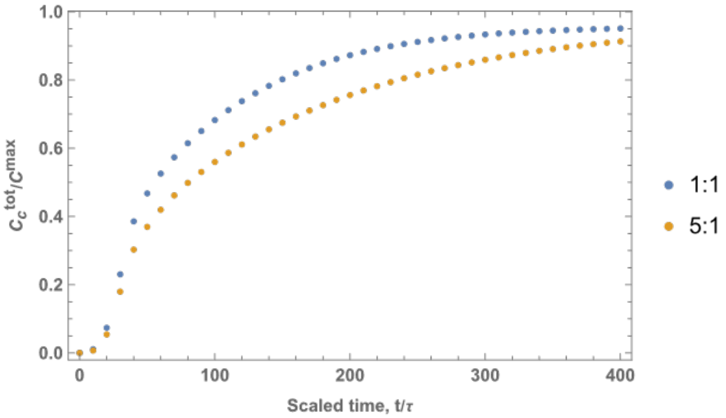

Fig. 4.7. The normalized concentration of C atoms, $C_C^{tot}\,(t))$ versus time for diffusivity ratios $D_B/D_A = 1$ (blue points) and $D_B/D_A = 5$ and $k/D_A = 0.05$ (gold points).

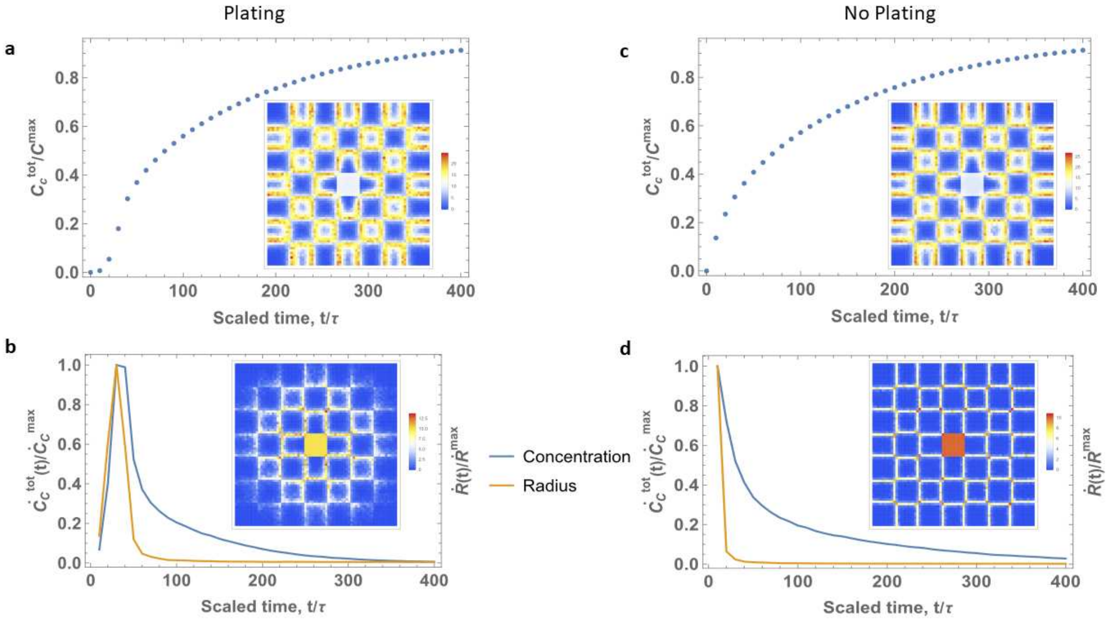

Fig. 4.8. The same as Fig. 4.4, except that $D_B/D_A = 5$ and $k/D_A = 0.05$. For the microstructural insets, the color range from red to blue indicates a range of C_C from high to low.

4.3 Discussion and Conclusion

Motivated by recent advances in the development of inhomogeneously patterned structures that subsequently react, we developed and validated here a reaction-diffusion formalism to model the microstructural evolution of a product phase produced via solid-state reaction. For concreteness, we considered two prototypical, initially bi-phasic templates whose temporal evolution illustrate a range of possible product microstructures. In the case of the single interface, the results were validated by comparison with a numerical integration of the governing equation. It was found that the template geometry, the kinetic parameters (i.e., diffusivities and reaction coefficients) and the product-phase stoichiometry dictated the morphologies of the final product microstructures.

As might have been anticipated, the initial morphology and distribution of the reactant phases provided a template for the microstructural evolution of the product phase. In the non-plating case, reaction occurred rapidly at all the bi-phase boundaries, creating a network of the product phase. As seen in Figs. 4, the rate of production of C then slows down, as the A and B atoms must traverse greater distances before they encounter their opposite number. In the case of plating and a centrally located "seed" of the C-phase, the network of product phase nucleates adjacent to the seed grain and extends radially outwards. Due to the plating constraint, a higher proportion of the C is formed at locations closer to the seed grain. The spatial distribution of C is also more diffuse in these locations (compared to the non-plating case), due to the relatively longer times available for growth. The simulation approach provides a highly flexible framework that can readily test the influence of different starting microstructures. These initial conditions could be hypothetical, or based on experimental microstructures. For starting cases where A and B exhibit a range of grain sizes, it is anticipated that the larger grains would result in remnant islands of the non-reacted phases. If such regions are widely separated, the production of C would effectively be halted. The potential also exists to modify the relative diffusion rates of the A and B species, as well as to adjust the diffusivities depending on the amount of C present. Clearly this latter modification is of relevance to experimental systems where the product phase could represent pathways of enhanced transport, or regions where diffusion is slowed.

The study showed that changing the stoichiometry of the product phase has a marked effect on the resultant microstructure. If the initial concentration of the reactants (A, B) is the same, then the local availability of the constituent with the higher concentration in the product phase (e.g. A for the product C= $\mathrm{A_2B}$) will control the degree of completion of a reaction. The reaction initiates at the bi-phase boundaries adjacent to the seed grain, and then proceeds laterally, with the C-phase preferentially growing into and consuming the A grains. The resultant microstructure comprises diffuse, ring-like regions of C. Interestingly, the concentration of C is lower at the original grid points, giving the rings the appearance of being unconnected.

In the next phase of this work our aim is to make a more quantitative connection between the simplified models discussed here and our experiments. To do this, we plan to solve the inverse problem of determining unknown experimental parameters, including diffusivities and reaction rates, from observed experimental microstructures utilizing the reaction-diffusion simulations. These microstructures can be acquired at different times in the process by a series of quenches. More specifically, we will digitize the starting duplex template and use this structure as the initial conditions in our simulations. We can then perform many simulations in parallel, each based on different rate assumptions, to compare the resultant synthetic product microstructures with those seen in experiment. To "zeroth order" our comparison will be based not on a detailed matching of pixels but, rather, on matching, for example, somewhat coarser descriptors, such as the moments of the spatial distribution product phase (e.g., the radius of gyration discussed in the manuscript). We expect that this comparison will probably not lead to a unique prediction of reaction and diffusion rates, but should permit us to eliminate many kinetic scenarios and to identify a relatively small subset of kinetic possibilities.

It is also of interest to consider the implications of our results for the design of desirable product microstructures. From the results presented here, one expects that these microstructures will be controlled, at least in part, by the diffusivity ratio, D_A/D_B, and magnitude of the difference in stoichiometric coefficients, $|m-n|$ for a given initial duplex structure. The diffusivity ratio can, in turn, be tuned to some degree by varying temperature when the reacting species have different activation energies for diffusion. Moreover, one can quench an evolving microstructure at some point during its evolution to select a particular pattern. Moreover, the initial duplex structure can also be tuned to bias the product microstructures. The realization of experimentally desired product microstructures by these various routes is also the subject of ongoing investigations.

Finally, it should be noted that the reaction-diffusion model for microstructure described here has rather broad application. As discussed in the introduction, a focus of the model has been the solid state reaction between the components of a duplex microstructure, which is a process widely utilized for a broad range of complex ceramic materials. It is envisaged that the model would be particularly pertinent to systems where the product phase has electronic or physical properties that differ markedly from the starting components, since the morphology of the reactant phase network will have significant implications as to the overall properties. Moreover, the plating/non-plating aspect directly addresses the epitaxial nature of many interfacial reactions. As such, we believe our microstructure based approach has utility for a broad range of applications. The model is also directly applicable to the situation where a material with a eutectoid microstructure is heated to a temperature greater than the eutectic temperature, and the reverse eutectoid reaction takes places, i.e., $\alpha + \beta \rightarrow \gamma$. This process can be exploited to modify the microstructure to achieve increase corrosion resistance in nickel-aluminum bronzes [81]. More generally, the model framework can readily be adapted to study different types of reactions in two phase materials. For example, there is a great deal of research into lead free solders for electronic packaging. Most of the candidate replacement alloys are based on eutectic compositions. One of the major technological challenges in these systems is that reaction of one (or more) of the eutectic phases with the metallization layers can lead to the formation of intermetallic compounds that are deleterious to the electrical conductivity and adhesion of the solder joint [82,83]. Clearly, the model could be adapted to study the diffusion of the metallization and solder elements, and their subsequent reaction to form the intermetallic phase.

Chapter 5

Interacting Fronts in a Model of Entropy-Stabilized Reactive Phase Formation

5.1 Introduction

Solid-state reactions are widely exploited for the synthesis of complex materials, including those used in the microelectronics industry [84,85] and a variety of ceramics having structural and electronic applications [56,58,59,66–69]. The kinetics of such reactions are often dictated by starting geometries that promote subsequent phase formation between, for example, thin films and substrates [59, 62], and reactant-phase powder particles [67–69]. For idealized geometries (e.g., planar interfaces), different quantitative reaction kinetics models of phase formation have been advanced, such as those developed by Wagner [72] and Schmalzried [73, 74], while simulational approaches, such as cellular automata (CA), have been employed to describe physico-chemical phenomena [42,43,75].

The aforementioned models can often be described using the formalism of a reaction-diffusion process in which the constituent reactants are transported via diffusion with subsequent product-phase formation. For simplicity, consider the process $A + B \rightarrow C$ that initiates at a planar interface at time $t = 0$. It is of particular interest to characterize the propagation of the resulting product-phase front as it effectively determines the temporal dependence of the transformation fraction. Gálfi and Rácz [77] examined quantitatively the dynamics of an idealized planar reaction-diffusion front in the mean-field approximation, focusing in particular on long-time behavior. Schenkel *et al.* [86] re-examined the asymptotics of the solution to this problem to highlight issues relating to the convergence of the solution to the scaling limit. Somewhat later Taitelbaum *et al.* [79] applied perturbation theory to the same system to obtain, to first order in the perturbation parameter, the local rate of product-phase formation. More generally, we note that the study of pattern formation in reacting-diffusing systems originated with the early work of Turing who examined the creation of so-called Turing patterns that develop from homogeneous systems due to an instability [87].

Despite the technological importance of solid-state reactions in materials processing, the connection between an initial, reactant microstructure and the ensuing kinetics has been relatively little studied until quite recently. For example McNamara *et al.* modeled the microstructural evolution of the product phase resulting from a solid-state reaction initiated at a bi-phasic template. More specifically, they connected the spatio-temporal evolution of the product phase with the geometry and chemistry of the starting duplex structure by employing a technique developed for chemical systems and generalized to incorporate microstructural evolution [51, 53, 88]. Our aim here is to employ this model to examine quantitatively the propagation and interaction of evolving product-phase fronts that characterize this prototypical system. As will be seen below, the interaction between two such fronts is key to understanding the kinetics of the transformation.

While we have been interested in formulating general models of reactive-phase formation starting from a prescribed template, the other motivation for this effort is the interpretation of our ongoing studies of product-phase formation in systems having entropy-stabilized line compounds that are thermodynamically stable only above a certain critical temperature. One such system is Co-Ti-O, which contains the entropy stabilized composition cobalt dititanate, $CoTi_2O_5$ [6, 31, 76] that may be promoted via a high-temperature heat treatment. Of particular interest here is the possibility of single crystal generation of a product phase via solid-state synthesis, a novel prospect that has only recently been reported in ceramic systems. With this in mind, we finally discuss the application of the aforementioned reaction-diffusion model to the interpretation of phase formation kinetics in the Co-Ti-O system.

5.2 Methodology

Two related transformation scenarios, each initiating with a bi-phasic α/β structure, will be considered here, as illustrated in Figs. 5.1 [89]. In Scenario 1, A (B) atoms that are initially separated and each uniformly distributed interdiffuse at a series of parallel phase boundaries that terminate at a seed layer comprising C atoms and react to produce immobile C atoms when both A and B atoms are in proximity to C atoms in stoichiometric (here $1:1$) proportions. It is assumed C production is described by a second-order reaction with rate constant k. In this model, both A and B atoms have the same diffusivity D, the C atoms are immobile and proximity represents a plating condition in which the reacting atoms are in or near a pixel containing a threshold number of C atoms (usually taken to be one). In Scenario 2, the phase boundaries are taken to be high-diffusivity paths (having diffusivity D') relative to the bulk (having diffusivity D) and are modeled as thin channels that may be initially empty (or not) and into which reactant atoms may migrate. The production of immobile C atoms then occurs when the diffusants reach the seed in equal proportions. Scenario 2 is akin to discontinuous dissolution reaction in which a migrating front tracks the evolution of a system from a two-phase structure to a single-phase structure. In both scenarios, the interdiffusion of reactant atoms produces a front that, owing to the plating conditions, results in a propagating product-phase front that comprises C atoms.

The results obtained from the simulations will be given for a single phase boundary, and so there is an additional average over the statistically identical boundaries. We will be interested in the net production of C over time associated with both scenarios described above and the identification of important kinetic regimes. For this purpose, it is useful to classify the results for Scenario 1 in terms of the diffusive Damköhler number, $Da = kC_0\ell^2/D$, where the initial concentration $C_0 = N/\ell^2$ for either A or B atoms and the mean diffusive transition rate $\Gamma = 4D/\ell^2$, and for Scenario 2 in terms of the diffusivity ratio, $\Delta = D'/D$. The Damköhler number quantifies the relative importance of the reaction and diffusion kinetics [90].

5.3 Results

5.3.1 Product-Phase Production For Reaction-Diffusion Model With Plating: Scenario 1

Simulation Results

In this scenario, atoms of type A and B interdiffuse at phase boundaries and then produce C via a second-order reaction. This process may be visualized by examining Figures 5.2 that show the advance of the product-phase front for times $t = 100\tau$ and 600τ. At the earlier time, it can be seen that two fronts propagate towards each other due to the imposed periodic boundary conditions with a spatial variation in C production along the z-direction

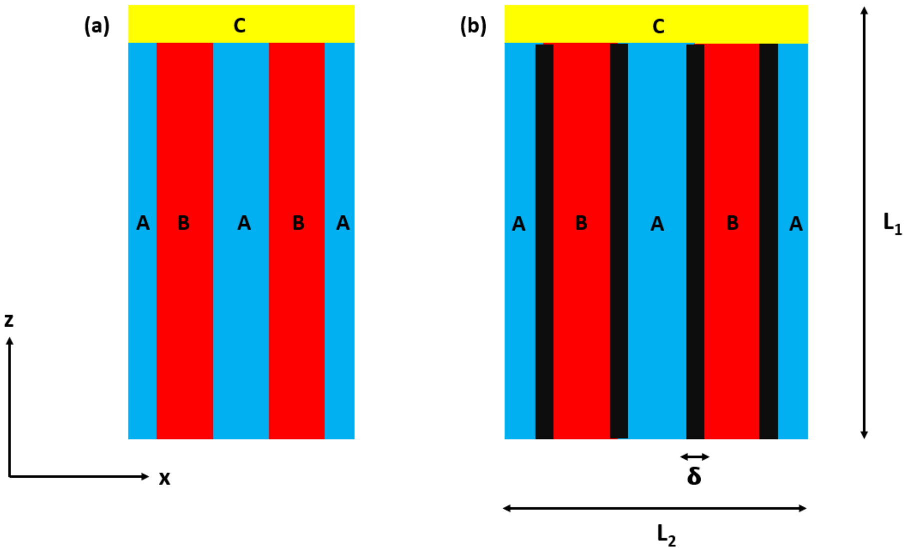

Fig. 5.1. a.) A schematic of Scenario 1 in which A and B atoms interdiffuse at a series of parallel phase boundaries, each of which terminates at a seed layer comprising immobile C atoms. b.) A schematic of Scenario 2 in which the phase boundaries of width δ are taken to be high-diffusivity paths relative to the bulk and are modeled initially as thin channels that may be empty or not and into which reactant atoms may migrate. For both scenarios, the product of C atoms occurs when reactants are in proximity to C atoms (the plating condition).

due to the plating condition. At the later time, these fronts have impinged, and C production continues along the original interface so as to smooth out existing spatial variations in C. From these considerations, it is convenient to regard product-phase production as comprising, broadly speaking, two temporal regimes, namely pre- and post-impingement, as will be evident from a description of the associated reaction kinetics.

The reaction kinetics for Scenario 1 is summarized in Figure 5.3a which presents the amount of C produced relative to the maximum possible amount, $\bar{C}_C\left(t\right)$, as a function of reduced time, t/τ, for several values of the Damköhler number, Da. As is evident from the figure, C production increases with decreasing Da and that, for a given Da, there are roughly two kinetic regimes separated by a transition time, t_c, that decreases with decreasing Da. This direct relationship between t_c and Da is expected since greater diffusivities for a given reaction rate (i.e., smaller Da) will result in enhanced interdiffusion with a concomitant increase in the speed of the propagating C front and therefore earlier transition times. The speed of the propagating C front may be deduced from Fig. 5.4 which displays the fractional position of the front along the z-direction, $\kappa\left(t\right)$, as a function of t. Clearly, the front speed, $v\left(t\right) = d\kappa/dt$, increases with decreasing Da, as expected, reaching a limiting constant of one pixel length per unit time, namely ℓ/τ - the maximum value given the lattice and time constraints.

Figure 5.3b is a log-log plot of $\bar{C}_C\left(t\right)$ versus t/τ that highlights the two kinetic regimes for Da small. The functional form for $\bar{C}_C\left(t\right)$ at early times is discussed further below where it is shown that, prior to front impingement, $\bar{C}_C\left(t\right) \propto t^{5/2}$. After front impingement, C production along the initial phase boundaries evolves to an eventual steady-state at late times in which the incoming reactant flux is balanced by a decrease in reactants that attends product formation. In this limit, $\frac{\partial C_A}{\partial t} = \frac{\partial C_B}{\partial t} \approx 0$, and therefore, since $\partial C_C/\partial t \propto C_A C_B$, $\bar{C}_C\left(t\right) \propto t$. This behavior is consistent with the data presented in the figure.

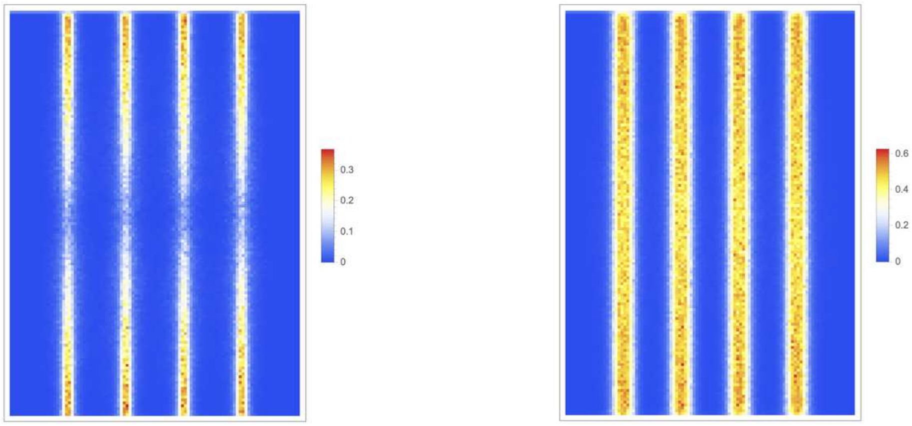

Fig. 5.2. The advance of the product-phase front for times $t = 100\tau$ (left) and 600τ (right) for Scenario 1. The color scale reflects the concentration of C atoms relative to the initial concentration of either A or B atoms. The system dimensions are $L_1 = 140$ and $L_2 = 100$. The results have been averaged over $\mathcal{M} = 30$ runs.

Analysis: Scenario 1

To describe the time-dependence of the propagating reaction in terms of reactant interdiffusion and incorporate the aforementioned plating condition, suppose that a reaction initiates at time t_i at a position $z_i\left(t_i\right)$ corresponding to the location of existing C atoms such that the rate of production of C is given by

$$\frac{\partial C_C\left(x,z,t\right)}{\partial t} = k\left(t-t_i\right) C_A\left(x,z,t\right)\ C_B\left(x,z,t\right). \tag{5.1}$$

(See Fig. 5.1a for a schematic of the simulation cell.) We take $k\left(t-t_i\right) = k\Theta\left(t-t_i\right)$, where $\Theta(x)$ denotes a step function.

For Da small (D large), one can obtain the rate of production of C due to interdiffusion using perturbation theory [79] in terms of the solutions to the diffusion equation for C_A and C_B in the absence of a reaction. Given that the initial concentrations are given by

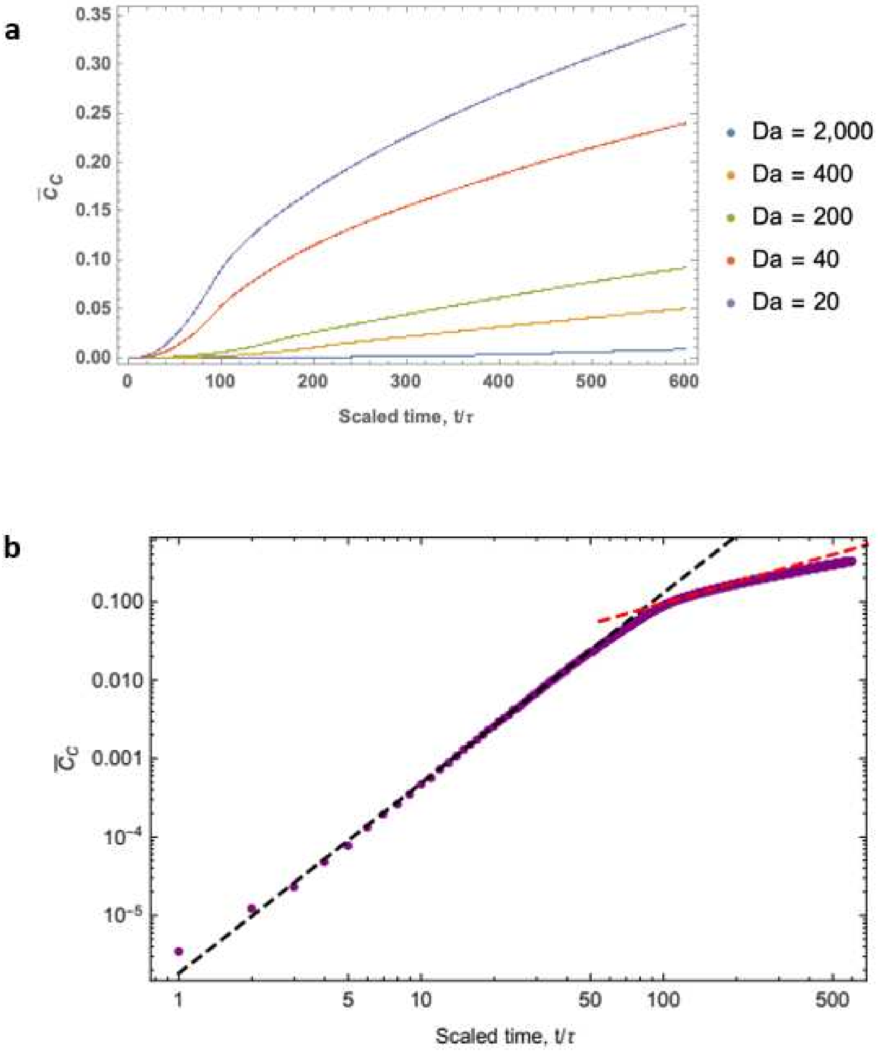

Fig. 5.3. a.) The normalized amount of C produced, $\bar{C}_C\,(t)$, as a function of reduced time, t/τ, for several values of the Damköhler number, Da for Scenario 1. The results have been averaged over $\mathcal{M} = 30$ runs. b.) A log-log plot of $\bar{C}_C\,(t)$ versus t/τ highlighting the two kinetic regimes for $Da = 20$. The dashed lines are power-law fits to the curves in the two kinetic regimes as obtained from an analysis of the kinetic behavior, the black (red) line having a slope of 2.42 (0.89).

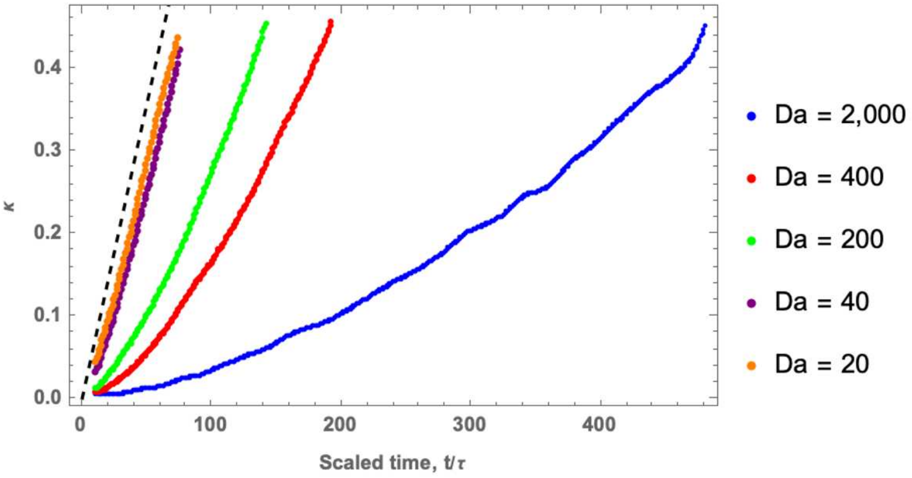

Fig. 5.4. The fractional position of the front along the z-direction, $\kappa(t)$, as a function of t for several values of Da. The results have been averaged over $\mathcal{M} = 30$ runs. The dashed line corresponds to propagation with the limiting speed of one pixel length per unit time (ℓ/τ). The curves have been smoothed for ease of reading.

$C_A(x,0) = c_0\Theta(x)$ and $C_B(x,0) = c_0(1-\Theta(x))$, one finds that

$$\begin{aligned} C_A(x,t) &= \frac{c_0}{2}\left[1+\operatorname{erf}\left(\frac{x}{2\sqrt{Dt}}\right)\right], \\ C_B(x,t) &= \frac{c_0}{2}\left[1-\operatorname{erf}\left(\frac{x}{2\sqrt{Dt}}\right)\right], \end{aligned} \tag{5.2}$$

where erf is the error function. Then, the local rate of C production may be obtained to first order in Da by

$$R(x,z,t) \approx k(t-t_i)\left(\frac{c_0}{2}\right)^2 \left[1-\operatorname{erf}\left(\frac{x}{2\sqrt{Dt}}\right)^2\right] \approx k(t-t_i)\left(\frac{c_0}{2}\right)^2 \exp\left[\frac{-\pi^2x^2}{32Dt}\right], \tag{5.3}$$

where the square of the error function has been approximated in terms of a Gaussian.

Suppose that when the A and B atoms interdiffuse an interfacial layer of width $2q$ is created about $x = 0$. Then, for a given position z_i that becomes active at time t_i, the rate of

C production associated with this layer is

$$f\left(t, t_i, q\right) = k\Theta\left(t - t_i\right)\left(\frac{c_0}{2}\right)^2 \int_{-q}^{+q} dx\ \exp\left[\frac{-\pi^2 x^2}{32Dt}\right] =$$

$$kc_0^2\sqrt{\frac{2D}{\pi}}\left[\sqrt{t}\,\mathrm{erf}\left(\frac{\pi^2 q}{32\sqrt{Dt}}\right) - \sqrt{t_i}\,\mathrm{erf}\left(\frac{\pi^2 q}{32\sqrt{Dt_i}}\right)\right]\ \Theta\left(t - t_i\right) \tag{5.4}$$

Thus, for reactions initiating at multiple times, the total rate of production of C is $\sum_i f\left(t, t_i, q\right)$.

Next, suppose that the initiation times are linked to the positions z_i by a constant speed v such that $z_i = vt_i$ corresponding to a moving front. From the results given above, propagation of the front at constant speed $v = \ell/\tau$ is associated with Da large. If the positions are taken instead as a continuous variable occurring with a constant density ρ, then we can obtain the total rate of production of C via

$$R_{TOT}\left(t\right) =$$

$$k\rho c_0^2\sqrt{\frac{2D}{\pi}}\int_0^\infty dz_i\ \left[\sqrt{t}\,\mathrm{erf}\left(\frac{\pi^2 q}{32\sqrt{Dt}}\right) - \sqrt{z_i/v}\,\mathrm{erf}\left(\frac{\pi^2 qv}{32\sqrt{Dz_i}}\right)\right]\ \Theta\left(t - z_i/v\right) =$$

$$k\rho c_0^2\sqrt{\frac{2D}{\pi}}\int_0^{vt} dz_i\ \left[\sqrt{t}\,\mathrm{erf}\left(\frac{\pi^2 q}{32\sqrt{Dt}}\right) - \sqrt{z_i/v}\,\mathrm{erf}\left(\frac{\pi^2 q}{32\sqrt{Dz_i/v}}\right)\right] \tag{5.5}$$

The result is

$$R_{TOT}\left(t\right) = k\rho c_0^2\sqrt{\frac{2D}{3\pi}}vt^{3/2}\left[\mathrm{erf}\left(\frac{\alpha q}{\sqrt{Dt}}\right) + g\left(\frac{q}{\sqrt{Dt}}\right)\right], \tag{5.6}$$

where

$$g\left(\frac{q}{\sqrt{Dt}}\right) = \frac{2\alpha}{\sqrt{\pi}}\frac{q}{\sqrt{Dt}}\left[\exp\left(-\frac{\alpha^2 q^2}{Dt}\right) - \frac{\alpha^2 q^2}{Dt}\Gamma\left(0, \frac{\alpha^2 q^2}{Dt}\right)\right], \tag{5.7}$$

Γ is the incomplete gamma function and $\alpha = \frac{\pi^2}{32}$.

For simplicity, consider the thick-interface limit $q \to \infty$. In this limit, one finds that

$$\bar{C}_C\left(t\right) \propto R_{TOT}\left(t\right) \to k\rho c_0^2\sqrt{\frac{2D}{3\pi}}vt^{3/2} \tag{5.8}$$

since

$$\begin{aligned} \lim_{q\to\infty} \operatorname{erf}\left(\frac{\alpha q}{\sqrt{Dt}}\right) &= 1, \\ \lim_{q\to\infty} g\left(\frac{q}{\sqrt{Dt}}\right) &= 0. \end{aligned} \tag{5.9}$$

So, in this limit, the total C production until time t is

$$\int_0^t dt' \; R_{TOT}\left(t'\right) \propto t^{5/2} \tag{5.10}$$

This description of the total C production is valid until the impingement of the fronts propagating towards one another. After that, as described above, C production occurs along the original interface normal to x axis (see Fig. 5.3b).

5.3.2 Product-Phase Production For Dissolution Model: Scenario 2

Simulation Results

In this scenario, phase boundaries are taken to be high-diffusivity paths relative to the bulk and are modeled as thin channels of width δ that may be initially empty or filled and into which reactant atoms may migrate (see Fig. 5.1b). The production of immobile C atoms at the seed location occurs when the diffusants reach this location in equal proportions. This movement of diffusants results in an augmentation of the seed due to the plating of product atoms and the diffusivity ratio, $\Delta = D'/D$, is the relevant control parameter here.

Consider first the case in which the boundary channel is initially empty. The movement of the seed boundaries requires a net transition of both A and B atoms into the channel and their subsequent migration to the seed. If, on the other hand, the boundary is initially full and contains the same proportion of A and B atoms as in the bulk, then some of these

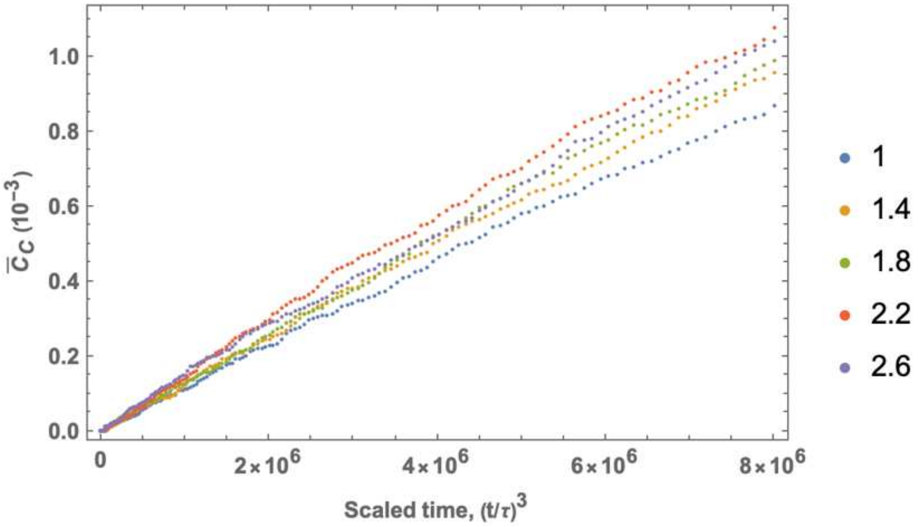

Fig. 5.5. The relative amount of C production at the seed, $\bar{C}_C\,(t)$ versus $(t/\tau)^3$ for the empty-channel case for a (bulk) Damköhler number, $Da = 0.8$, and various diffusivity ratios, Δ (as shown in the legend). These results are for Scenario 2 and have been averaged over $\mathcal{M} = 30$ runs. The simulation cell dimensions are $L_1 = 140$ and $L_2 = 88$ and the channel width $\delta = 2$.

additional atoms will migrate to the seed, and it is expected that plating will occur more rapidly than in the empty-channel case. To compare and contrast these two cases, it is convenient to characterize the migration process in terms of the time-dependence of the relative amount of C produced, $\bar{C}_C\,(t)$ at the seed, where the reference state here is, again, the total possible C production.

Figure 5.5a shows the time evolution of $\bar{C}_C\,(t)$ for the empty-channel case for a fixed (bulk) Damköhler number, $Da = 0.8$, and various diffusivity ratios, Δ. It should be noted that, for the empty-channel case, $\bar{C}_C\,(t)$ increases approximately as t^3, as expected from the analysis provided below. Finally, Fig. 5.6 compares the time evolution of $\bar{C}_C\,(t)$ for $\Delta = 2.6$ and a bulk $Da = 0.8$ for both the empty- and full-channel cases showing, as expected, that the full-channel case leads to enhanced product production at the seed. Further discussion of this result will be given in the Analysis subsection below.

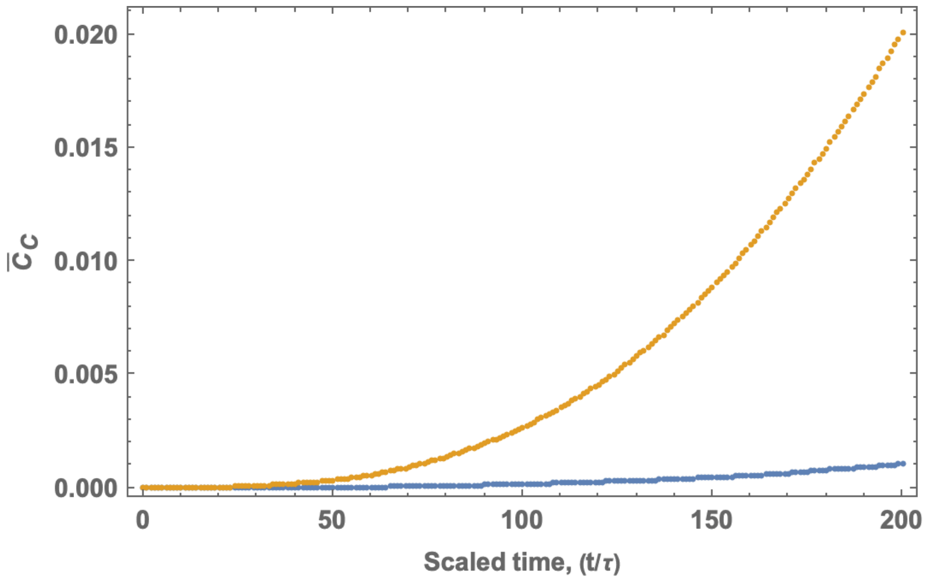

Fig. 5.6. The time evolution of $\bar{C}_C\,(t)$ for $\Delta = 2.6$ and a bulk $Da = 0.8$ for both the empty- (blue curve) and full-channel (gold curve) cases.

Analysis: Scenario 2

The rate of C produced at the seed can be obtained for the full channel case from analytical solutions to an idealized grain-boundary diffusion problem. Harrison [91] considered the case of outward mass diffusion at a grain boundary of width δ aligned normal to a surface at $z = 0$ and obtained the associated flux from a modification of Whipple's solution [92] to a related problem. However, these analyses are predicated on the assumption that $\Delta >> 1$ [93], and so we employ instead an approximate treatment that highlights the main contributions to the rate of C production.

To simplify the analysis of the two-dimensional geometry of the simulation, consider a one-dimensional single phase boundary channel of length L of width δ subject to periodic boundary conditions along z. In this picture diffusion occurs outward towards the seed at $z = 0$ and $z = L$ and atoms injected from the external bulk are modeled as a time-dependent source. (We note that bulk diffusion will not be effective in producing C at the seed in the simulation given the spatial separation of diffusants A and B.) We can then write for the channel that

$$\frac{\partial C_A\left(x,z,t\right)}{dt} = D' \frac{\partial^2 C_A}{\partial z^2} + Q\left(z,t\right), \tag{5.11}$$

where the source term $Q\left(z,t\right)$ embodies the flux of A atoms injected into the channel from the surrounding bulk region. We assume that the source term is independent of z so that $Q\left(z,t\right) = Q\left(t\right)$. Similar equations can be written for C_B. When A and B atoms both reach the seed in equal proportions they can react to produce C atoms.

The solution to Eq. (5.11) with absorbing boundary conditions at $z = 0$ and L, namely $C_A(0,t) = C_A(L,t) = 0$, and an initial distribution of A atoms, $C_A\left(z,0\right)$, is given by

$$C_A\left(z,t\right) = \int_0^L dz' \int_0^t dt'\; G\left(z,t;z',t'\right) Q\left(t'\right) + \int_0^L dz'\; C_A\left(z',0\right) G\left(z,t;z',0\right), \tag{5.12}$$

where $G\left(z,t;z',t'\right)$ is the Green function [94]. The Green function [95] is

$$G\left(z,t;z',t'\right) = \frac{2}{L}\sum_{n=1}^{\infty} \sin\left(\frac{n\pi z'}{L}\right) \sin\left(\frac{n\pi z}{L}\right) \exp\left[-D'\left(\frac{n\pi}{L}\right)^2 \left(t-t'\right)\right] \tag{5.13}$$

It is convenient to consider first the empty-channel case where $C_A\left(z,0\right) = 0$ and carry out the integration of the Green function in the first integrals over z'. One finds that

$$\int_0^L dz'\; G\left(z,t;z',t'\right) = \frac{4}{\pi}\sum_{n\ odd} \left(\frac{1}{n}\right) \sin\left(\frac{n\pi z}{L}\right) \exp\left[-D'\left(\frac{n\pi}{L}\right)^2 \left(t-t'\right)\right], \tag{5.14}$$

and so

$$C_A\left(z,t\right) = \frac{4}{\pi}\sum_{n\ odd} \left(\frac{1}{n}\right) \sin\left(\frac{n\pi z}{L}\right) \int_0^t dt' \exp\left[-D'\left(\frac{n\pi}{L}\right)^2 \left(t-t'\right)\right] Q\left(t'\right) \tag{5.15}$$

With this information one can determine the flux, $F\left(t\right)$, of A atoms at $z = 0$ and $z = L$

given by

$$F(t) = -D' \frac{\partial C_A}{\partial z}|_{z=0} = \\ -\frac{4D'}{L} \sum_{n\ odd} \exp\left(-D'\left(\frac{n\pi}{L}\right)^2 t\right) I(t), \tag{5.16}$$

where

$$I(t) = \int_0^t dt' \exp\left(D'\left(\frac{n\pi}{L}\right)^2 t'\right) Q(t'). \tag{5.17}$$

To perform the final integral, consider the injection of atoms from the bulk into the channel. We can approximate the source term by using the flux of atoms associated with the initial bulk concentration at channel boundaries. Thus,

$$Q(t) \approx \frac{c_0}{2L}\sqrt{\frac{D}{\pi t}} \tag{5.18}$$

Then,

$$I(t) = \frac{c_0}{2L}\sqrt{\frac{D}{\pi}} \int_0^t dt' \frac{\exp\left(D'\left(\frac{n\pi}{L}\right)^2 t'\right)}{\sqrt{t'}} = \\ \frac{c_0}{2}\sqrt{\frac{D}{D'}}\left(\frac{1}{n\pi}\right) \mathrm{erfi}\left(\frac{n\pi}{L}\sqrt{D't}\right), \tag{5.19}$$

where erfi denotes the imaginary error function. The imaginary error function is defined in terms of the usual error function, erf, by $\mathrm{erfi}(w) = -i\mathrm{erf}(iw)$. Putting everything together, the flux can be written as

$$F(t) = -\sqrt{D'D}\left(\frac{2c_0}{\pi L}\right) \sum_{n\ odd} \frac{1}{n} \exp\left(-D'\left(\frac{n\pi}{L}\right)^2 t\right) \mathrm{erfi}\left(\frac{n\pi}{L}\sqrt{D't}\right). \tag{5.20}$$

The total amount of A entering the seed at $z=0$ may be obtained from the integral

$$N_A\left(t\right)=\int_0^t d\tilde{t}\;F\left(\tilde{t}\right)=-\sqrt{D'D}\left(\frac{4c_0\bar{t}}{L\pi^{3/2}}\right)\sum_{n\;odd}\left[\frac{1}{n^2}\sqrt{\frac{t}{\bar{t}}}-\frac{1}{n^3}\,\mathcal{D}\left(n\sqrt{\frac{t}{\bar{t}}}\right)\right], \quad (5.21)$$

where $\bar{t}=\frac{L^2}{\pi^2 D'}$ and $\mathcal{D}$ is the Dawson function. The total amount of B entering the seed $N_B\left(t\right)=N_A\left(t\right)$.

The rate of C produced at the seed should be proportional to $N_A\left(t\right)N_B\left(t\right)$ such that

$$\frac{\partial C_C}{\partial t}=kN_A\left(t\right)N_B\left(t\right). \quad (5.22)$$

Since $\bar{t}$ is large for the simulation parameters, the relevant range of times is $t/\bar{t}$ small and one finds, to a good approximation, that $N_A\left(t\right)N_B\left(t\right)\propto t^2$ so that $C_C\propto t^3$ in this regime. This result is consistent with the data shown in Fig. 5.5. Finally, for the case of the full channel, the additional contribution to C production can be calculated using the second term of the right-hand side of Eq. (5.12).

5.4 Discussion and Conclusion

We performed modified stochastic computer (so-called τ-leaping) simulations of a simplified reaction-diffusion model of templated growth of a product phase formed by solid-state reaction between two reactant phases. In these simulations and the subsequent quantitative analyses of the associated kinetic equations, we focused on the propagation and interaction of evolving fronts that dictate the dynamic pathway of a solid-state reaction. Our aim was to link front propagation with the geometry of the initial, reactant microstructure for two reaction scenarios. From these studies, a consistent picture emerged that can be understood in limiting cases of the control parameters from approximations to the governing kinetic equations.

It is of interest to determine what this model can tell us about reactive phase formation in a system of some experimental interest, namely the Co-Ti-O system, a ternary ceramic that contains the entropy-stabilized pseudobrookite cobalt dititanate, $CoTi_2O_5$. In recent experimental work [6], two phases, namely $CoTiO_3$ and TiO_2, initially comprising a duplex microstructure reacted along the bi-phasic boundaries to form a product phase, $CoTi_2O_5$, that is stabilized by heat-treating at temperatures in excess of a critical temperature. To study the kinetics of this reaction, it is convenient to construct a seeded sample, analogous to that seen in Figs. 5.1, in which $CoTi_2O_5$ forms a thin layer on the top of a compressed compact.

From an analysis of the propagation of the reaction front in this system, it was found that, as with Scenario 1 described above, the reaction continues behind the moving front. In addition, one also observes in the experimental system the impingement of reacting fronts resulting from nucleation at opposing surfaces. (In the simulations this impingement follows, of course, from the imposed periodic boundary conditions.) Similar to the analysis performed above, it is also useful to track here the time-dependence of the fraction of product phase ($CoTi_2O_5$), $\phi(t)$, formed in the transformation. The results are shown in Fig. 5.7 for data acquired near the seed. The graphical analysis presented in the figure assumes a stretched-exponential functional form $\phi(t) = 1 - \exp(-at^n)$, and it is found from a fit to the data that the corresponding Avrami exponent $n = 0.61$. This value is roughly consistent with the kinetics associated with one-dimensional, diffusion-controlled growth in the absence of nucleation events, for which $n = 0.5$. It should be noted, though, that it is difficult to make a direct comparison between these experimental results and those obtained for the models above given the spatial limitations inherent in the experimental analysis. In short, more experimental data is needed both near to and far from the seed over a wider range of time scales than has been considered so far. However, the models described above provide a framework for the interpretation of these experimental efforts.

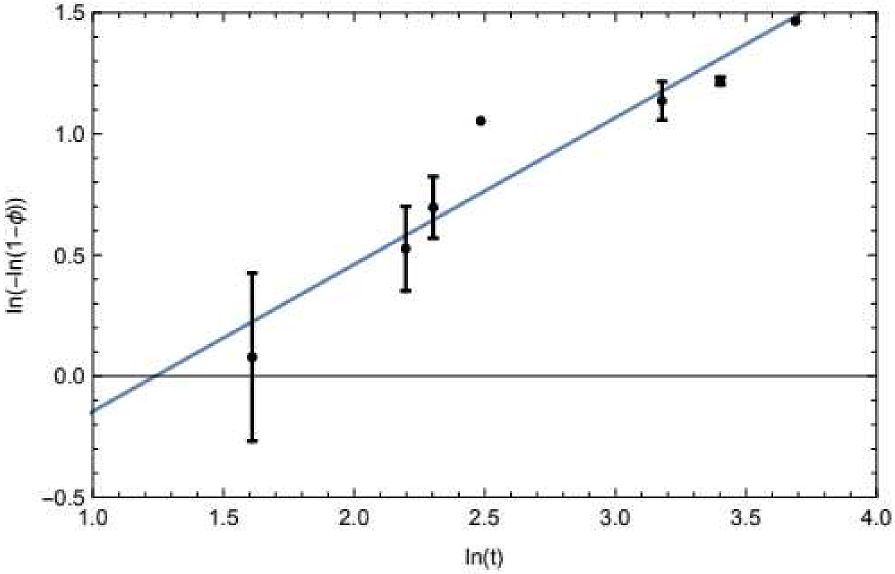

Fig. 5.7. The time-dependence of the fraction of product phase ($CoTi_2O_5$), $\phi\,(t)$, formed in the transformation in the Co-Ti-O system. The line is a fit to the experimental data. From this fit it is found that the corresponding Avrami exponent is $n = 0.61$.

Chapter 6

Impact

6.1 Method Development

The τ-leaping algorithm had previously not been applied to any material growth system. This is a novel modeling approach for the kinetic model of grain growth that allows for more control over the simulation with less information needed about the physical system. This method allows for an easier implementation of dictated starting microstructures when compared to many of the popular simulation methods. The approach we developed allows full control of the starting grain pattern either by coding it in by hand or using visual data, such as an EBSD map, of a physical sample. Additionally, the simulation is solving simplified reaction and diffusion equations as functions of a Poisson distribution. This allows for this model to be applied to systems that have limited information known about them in terms of rates.

6.2 Insight into the method

The τ-leaping algorithm was validated in its application to solid-state systems and as such we then examined the effects of the different system parameters on the end resulting growth. These parameters include the microstructure design, the reaction rate, the diffusion rate, and the addition of grain boundary diffusion. These all outline how this methodology can be used as a tool to accurately model a system. By adjusting these variables, the user can begin to model new systems with limited laboratory experiments. Concurrently, the user will be able to gain insight into the physical system depending on how the parameters were changed to find parity between the simulation and experimentation.

6.3 Insight into the production of $CoTi_2O_5$

The development of this model has been progressing in tandem alongside laboratory experiments on the solid-state synthesis reaction of $CoTiO_3$ and TiO_2 to form $CoTi_2O_5$. The methods we chose to evaluate the change in the system for the model, such as pixels transformed into C, have influenced the evaluation of the physical samples. This is a result of the work to connect the model and experimental tests directly, but it is also a byproduct of the model being a rapid test that generated large amounts of data. The best practices were found form the simulation data. The simulation also has allowed us to make more informed decisions regarding expected results and the cause of said results. While the model is not a $1 : 1$ simulation of the reaction of $CoTiO_3$ and TiO_2, it has accomplished a goal of expediting the laboratory work and furthering our understanding of this novel system.

Chapter 7

Future Work

7.1 Predictive Model

The model has been developed to simulate a solid-state reaction that mimics the reaction kinetics of the production of $CoTi_2O_5$. As noted, there is currently some limited parity between the model and the experimental data. While limited, the data does demonstrate that the model can be tuned to more accurately represent the experimental reaction. With this accurate model, the resulting microstructure of the solid-state reaction will be able to be predicted from the simulation.

This will be approached on two fronts: collection of more experimental data and connecting the model to physical parameters. The experimental data from the reaction of $CoTiO_3$ and TiO_2 to form $CoTi_2O_5$ is currently limited in terms of reaction rate and diffusion rate of the species. This data is useful in expediting the process of correlating the rates in the model to the physical values. Similarly the time in the model is currently unitless as it does not have a direct relation to an experimental timescale. The equations developed for the rate of production in the model are key to bridging the physical and simulated systems.

7.2 Machine Learning

In addition to the traditional method of collecting more experimental data, a parallel method to refine the model can be accomplished via machine learning. The common approach for utilizing machine learning on grain growth is to apply a generative adversarial network (GAN) to a training data set of initial and final microstructures with their corresponding input parameters [96]. Other methods have been applied, but they generally are searching for a solution without addressing the kinetics of the growth [97, 98]. Thus, a novel approach would be to apply machine learning techniques to refine the variables in the model. Utilizing a series of results from the model and some basic starting microstructures with the results from laboratory experiments one can train a model. The machine learning model could determine the optimal variables in the τ-leaping algorithm to achieve desired microstructures. With a fully trained model, the user will be able to know the physical settings and initial microstructure for their desired end result.

7.3 Curved Grains

The current model has only been applied to systems with square microstructures and straight lines. This is a limitation caused by the pixel density in model. The resolution of the model can be increased in the same was an that of an image, by increasing the pixel density. This is a computationally intensive solution as more pixels increase the number of calculations in each run as well as increasing the size of the data that must be stored and updated. As such this is not an ideal solution, but this has been solved in cellular automation models. In the work of Raghavan and Sahay, they were able to predict topology and track the curvature during the simulation [9]. This work utilized height functions for each cell in the simulation. Their model was not as complex, as it was only recrystallization and as such it was only dealing with multiple grains of one species. A variation of this approach could be applied to the general model developed. In their work the grain boundary velocity was determined by the net pressure, whereas in the τ-leaping algorithm it could be based on reacting species in close proximity.

References

[1] W. Zulehner. Czochralski growth of silicon. *Journal of Crystal Growth*, 65(1):189–213, 1983.

[2] D. Elwell. *Fundamentals of Flux Growth*, pages 133–142. Springer US, 1989.

[3] F. Rosenberger. *Fundamentals of Crystal Growth from Vapors*, pages 107–118. Springer US, 1989.

[4] Y. Liu, M. Militzer, and M. Perez. Phase field modelling of abnormal grain growth. *Materials*, 12, 2019.

[5] A. Khan, E.P. Gorzkowski, A.M. Scotch, E.R. Leite, T. Li, H.M. Chan, and M.P. Harmer. Influence of excess pbo additions on $\{111\}$ single-crystal growth of $Pb(Mg_{1/3}Nb_{2/3})O_3$–35 mol% $PbTiO_3$ by seeded polycrystal conversion. *Journal of the American Ceramic Society*, 86:2176–2181, 2003.

[6] K.P. Anderson, A.K. Giri, R.P. Vinci, and H.M. Chan. Single crystal growth of $CoTi_2O_5$ by solid state reaction synthesis. *Journal of the American Ceramic Society*, 102(9):5050–5062, 2019.

[7] A. Mirwan, S. Susianto, A. Altway, and R. Handogo. A modified shrinking core model for leaching of aluminum from sludge solid waste of drinking water treatment. *International Journal of Technology*, 8:19–26, 2017.

[8] F. Han. Cellular automata modeling of ostwald ripening and rayleigh instability. *Materials (Basel)*, 11, 2018.

[9] S. Raghavan and S.S. Sahay. Modeling the grain growth kinetics by cellular automaton. *Materials Science and Engineering: A*, 445-446:203–209, 2007.

[10] M. Braginsky, V. Tikare, and E. Olevsky. Numerical simulation of solid state sintering. *International Journal of Solids and Structures*, 42(2):621–636, 2005.

[11] N.M. Angel and A. Basak. On the fabrication of metallic single crystal turbine blades with a commentary on repair via additive manufacturing. *Journal of Manufacturing and Materials Processing*, 4, 2020.

[12] B.R. Pamplin. *Crystal Growth*. Pergamon Press, Oxford, 1980.

[13] I.V. Markov. *Crystal Growth for Beginners: Fundamentals of Nucleation, Crystal Growth and Epitaxy*. World Scientific, 1995.

[14] X. Yu and D. Yang. *Growth of Crystalline Silicon for Solar Cells: Czochralski Si*, pages 129–174. Springer Berlin Heidelberg, 2019.

[15] C.B. Carter and M.G. Norton. *Ceramic Materials Science and Engineering*. Springer, 2007.

[16] G. Müller and J. Friedrich. Crystal growth, bulk: Methods. In *Encyclopedia of Condensed Matter Physics*, pages 262–274. Elsevier, 2005.

[17] Z. Fisk and J.P. Remeika. Chapter 81 growth of single crystals from molten metal fluxes. volume 12 of *Handbook on the Physics and Chemistry of Rare Earths*, pages 53–70. Elsevier, 1989.

[18] H.Y. Lee. 6 - development of high-performance piezoelectric single crystals by using solid-state single crystal growth (SSCG) method. In *Handbook of Advanced Dielectric, Piezoelectric and Ferroelectric Materials*, pages 158–172. Woodhead Publishing, 2008.

[19] C. Paorici and G. Attolini. Vapour growth of bulk crystals by PVT and CVT. *Progress in Crystal Growth and Characterization of Materials*, 48-49:2–41, 2004.

[20] W.W. Piper and S.J. Polich. Vapor-phase growth of single crystals of II–VI compounds. *Journal of Applied Physics*, 32(7):1278–1279, 1961.

[21] S.S. Rong, M.B. Faheem, and Y.B. Li. Perovskite single crystals: Synthesis, properties, and applications. *Journal of Electronic Science and Technology*, 19(2):100081, 2021.

[22] I. Milisavljevic and Y. Wu. Current status of solid-state single crystal growth. *BMC Materials*, 2, 2020.

[23] T. Kimura. Application of texture engineering to piezoelectric ceramics - a review. *Journal of the Ceramic Society of Japan*, 114:15–25, 2006.

[24] S.J.L. Kang, J.H. Park, S.Y. Ko, and H.Y. Lee. Solid-state conversion of single crystals: The principle and the state-of-the-art. *Journal of the American Ceramic Society*, 98:347–360, 2015.

[25] T. Li, A.M. Scotch, H.M. Chan, M.P. Harmer, S.E. Park, T.R. Shrout, and J.R. Michael. Single crystals of $Pb(Mg_{1/3}Nb_{2/3})O_3$–35 mol% $PbTiO_3$ from polycrystalline precursors. *Journal of the American Ceramic Society*, 81:244–248, 1998.

[26] P.T. King, E.P. Gorzkowski, A.M. Scotch, D.J. Rockosi, H.M. Chan, and M.P. Harmer. Kinetics of $\{001\}$ $Pb(Mg_{1/3}Nb_{2/3})O_3$–35 mol% $PbTiO_3$ single crystals grown by

seeded polycrystal conversion. *Journal of the American Ceramic Society*, 86:2182–2187, 2003.

[27] E.P. Gorzkowski, H.M. Chan, and M.P. Harmer. Effect of pbo on the kinetics of $\{001\}$ $Pb(Mg_{1/3}Nb_{2/3})O_3$–35 mol% $PbTiO_3$ single crystals grown into fully dense matrices. *Journal of the American Ceramic Society*, 89:856–862, 2006.

[28] K.P. Anderson, R.P. Vinci, and H.M. Chan. Novel metal–ceramic composite microstructures produced through the partial reduction of $CoTiO_3$. *Journal of Materials Science*, 53:8193–8210, 2018.

[29] Y. Suzuki and Y. Shinoda. Magnesium dititanate ($MgTi_2O_5$) with pseudobrookite structure: a review. *Sci Technol Adv Mater.*, 12, 2011.

[30] W.A. Deer, R.A. Howie, and J. Zussman. *Rock-forming Minerals*. Geological Society, 1978.

[31] K.T. Jacob and G. Rajitha. Role of entropy in the stability of cobalt titanates. *The Journal of Chemical Thermodynamics*, 42(7):879–885, 2010.

[32] J.H. Harding. Short-circuit diffusion in ceramics. *Interface Science*, 11:81–90, 2003.

[33] H. Ge and H. Qian. *Chemical Master Equation*, pages 396–399. Springer New York, 2013.

[34] J.L. Muñoz-Cobo and C. Berna. Chemical kinetics roots and methods to obtain the probability distribution function evolution of reactants and products in chemical networks governed by a master equation. *Entropy (Basel)*, 21, 2019.

[35] D.T. Gillespie. A rigorous derivation of the chemical master equation. *Physica A: Statistical Mechanics and its Applications*, 188:404–425, 1992.

[36] D.T. Gillespie. Stochastic simulation of chemical kinetics. *Annual Review of Physical Chemistry*, 58:35–55, 2007.

[37] C.W. Gardiner, K.J. McNeil, D.F. Walls, and I.S. Matheson. Correlations in stochastic theories of chemical reactions. *Journal of Statistical Physics*, 14:307–331, 1976.

[38] W.E. Garner. *Chemistry of the Solid State*. Butterworths Scientific Publications, 1955.

[39] A. Khawam and D.R. Flanagan. Solid-state kinetic models basics and mathematical fundamentals. *The Journal of Physical Chemistry B*, 110(35):17315–17328, 2006.

[40] S.S. Chandratreya, R.M. Fulrath, and J.A. Pask. Reaction mechanisms in the formation of PZT solid solutions. *Journal of the American Ceramic Society*, 64(7):422–425, 1981.

[41] T. Karapiperis and B. Blankleider. Cellular automation model of reaction-transport porcesses. *Physica D: Nonlinear Phenomena*, 78(1):30–64, 1994.

[42] A.C.J. de Korte and H.J.H. Brouwers. A cellular automata approach to chemical reactions; 1 reaction controlled systems. *Chemical Engineering Journal*, 228:172–178, 2013.

[43] D. Dab, A. Lawniczak, J.P. Boon, and R. Kapral. Cellular-automaton model for reactive systems. *Phys. Rev. Lett.*, 64:2462–2465, 1990.

[44] P.G. Seybold, L.B. Kier, and C.K. Cheng. Simulation of first-order chemical kinetics using cellular automata. *Journal of Chemical Information and Computer Sciences*, 37(2):386–391, 1997.

[45] J.R. Weimar and J.P. Boon. Class of cellular automata for reaction-diffusion systems. *Phys. Rev. E*, 49:1749–1752, 1994.

[46] M.P Anderson, D.J Srolovitz, G.S Grest, and P.S Sahni. Computer simulation of grain growth—I. kinetics. *Acta Metallurgica*, 32(5):783–791, 1984.

[47] Z. Jiang and C. Ebner. Dynamical monte carlo study of crystal growth in a solid-on-solid model. *Phys. Rev. B*, 40:4833–4837, 1989.

[48] H.M. Taylor and S. Karlin. *An Introduction To Stochastic Modeling*. Academic Press, 1998.

[49] N.S. Goel and N. Richter-Dyn. *Stochastic Models in Biology*. Academic Press, 1974.

[50] P. Érdi and G. Lente. *Stochastic Chemical Kinetics*. Springer, 2014.

[51] D.T. Gillespie. A general method for numerically simulating the stochastic time evolution of coupled chemical reactions. *Journal of Computational Physics*, 22(4):403–434, 1976.

[52] D.T. Gillespie. Exact stochastic simulation of coupled chemical reactions. *The Journal of Physical Chemistry*, 81(25):2340–2361, 1977.

[53] D.T. Gillespie. Approximate accelerated stochastic simulation of chemically reacting systems. *The Journal of Chemical Physics*, 115(4):1716–1733, 2001.

[54] J.M.A. Padgett. Adaptive time-stepping in the numerical solution of the reaction-diffusion master equation. Masters thesis, Ryerson University, 2012.

[55] J.M.A. Padgett and S. Ilie. An adaptive tau-leaping method for stochastic simulations of reaction-diffusion systems. *AIP Advances*, 6(3):035217, 2016.

[56] D. Segal. Chemical synthesis of ceramic materials. *J. Mater. Chem.*, pages 1297–1305, 1997.

[57] W.D. Kingery, H.K. Bowen, and D.R. Uhlmann. *Introduction to Ceramics, 2nd*. Wiley-Blackwell, 1976.

[58] A.R. West. *Solid State Chemistry and its Applications*. Wiley, 2014.

[59] P.G. Kotula and C.B. Carter. Interfacial control of reaction kinetics in oxides. *Phys. Rev. Lett.*, 77:3367–3370, 1996.

[60] P.G. Kotula and C.B. Carter. Nucleation of solid-state reactions between nickel oxide and aluminium oxide. *Journal of the American Ceramic Society*, 78:248–250, 1995.

[61] C.R. Gorla, W.E. Mayo, S. Liang, and Y. Lu. Structure and interface-controlled growth kinetics of $ZnAl_2O_4$ formed at the $(11\bar{2}0)$ ZnO / $(01 1\bar{2})$ Al_2O_3 interface. *Journal of Applied Physics*, 87:3736–3743, 2000.

[62] M.T. Johnson, P.G. Kotulat, R.S. Thompson, and C. Barry Carter. Solid-state reactions in model oxide systems. *Mat. Res. Soc. Symp. Proc.*, 453:695–701, 1997.

[63] L. Kril'ová and N. Števulová. The kinetic study of the synthesis of magnesium aluminate spinel from mechanochemically treated mixtures of oxide-hydroxide. *J. Mater. Sci.*, 39:5403–5405, 2004.

[64] E. Brzozowski and M.S. Castro. Synthesis of barium titanate improved by modifications in the kinetics of the solid state reaction. *Journal of the European Ceramic Society*, 20:2347–2351, 2000.

[65] T.Y. Wu and W.C.J. Wei. Transformation kinetics of $Ba_2Ti_9O_{20}$ with ZrO_2 additive. *J. Am. Ceram. Soc.*, 89:3846–3849, 2006.

[66] J. Koruza, J. Tellier, B. Malič, V. Bobnar, and M. Kosec. Phase transitions of sodium niobate powder and ceramics, prepared by solid state synthesis. *Journal of Applied Physics*, 108:113509, 2010.

[67] Y.P. Fu, C.C. Chang, C.H. Lin, and T.S. Chin. Solid-state synthesis of ceramics in the BaO-SrO-Al2O_3-SiO_2 system. *Ceramics International*, 30:41–45, 2004.

[68] M. Kracum, A. Kundu, M.P. Harmer, and H.M. Chan. Novel interpenetrating Cu-Al_2O_3 structures by controlled reduction of bulk $CuAlO_2$. *J. Mater. Sci.*, 50:1818–1824, 2015.

[69] R.R. Rao, H.N. Roopa, and T.S. Kannan. Solid state synthesis and thermal stability of HAP and HAP-β-TCP composite ceramic powders. *J. Mater. Sci.*, pages 511–518, 1997.

[70] P.W.M. Jacobs and F.C. Tompkins. *Classification and theory of solid reactions*, chapter 7. Academic Press, New York, 1995.

[71] S.S. Chandratreya. *Theoretical Aspects of Solid-State Reactions in a Mixed Particulate Ensemble and Kinetics of Lead Zirconate Formation*. PhD thesis, U.C. Berkeley, 1980.

[72] C. Wagner. Über den mechanismus von doppelten umsetzungen durch reaktion im festen zustand. *Zeitschrift für anorganische und allgemeine Chemie*, 236:320–338, 1938.

[73] H. Schmalzried. *Solid State Reactions*. Verlag Chemie International Inc, 2nd edition, 1981.

[74] H. Schmalzried. *Chemical Kinetics of Solids*. VCH, 1995.

[75] T. Karapiperis and B. Blankleider. Cellular automation model of reaction-transport porcesses. *Physica D*, 78:30–64, 1994.

[76] B. Brežný and A. Muan. Phase relations and stabilities of compounds in the system CoO-TiO_2. *J. Inorg. Nucl. Chem.*, 31:649–655, 1969.

[77] L. Galfi and Z. Racz. Properties of the reaction front in an A + B → C type reaction-diffusion process. *Phys Rev A Gen Phys*, 1988.

[78] B. Chopard and M. Droz. Microscopic studies of the properties of the reaction front in an a+b → c system reaction-diffusion process. *Europhys. Lett.*, 15:459–465, 1991.

[79] H. Taitelbaum et al. Some properties of the A + B → C reaction-diffusion system with initially separated components. *Journal of Statistical Physics*, 65, 1991.

[80] J. Rudnick and G. Gaspari. *Elements of the Random Walk: An Introduction for Advanced Students and Researchers*. Cambridge University Press, 2004.

[81] R. Cottam and M. Brandt. 20 - Laser surface treatment to improve the surface corrosion properties of nickel-aluminum bronze. In *Laser Surface Engineering*, pages 469–481. Woodhead Publishing, 2015.

[82] F.L. Lau, R. I Made, W.N. Putra, J.Z. Lim, V.C. Nachiappan, J.L. Aw, and C.L. Gan. Electrical behavior of au–ge eutectic solder under aging for solder bump application in high temperature electronics. *Microelectron. Reliab.*, 53:1581–1586, 2013.

[83] W. Tao, C. Chen, C.E. Ho, W.T. Chen, and C.R. Kao. Selective interfacial reaction between Ni and eutectic BiSn lead-free solder. *Chemistry of Materials*, 13:1051–1056, 2001.

[84] K. Barmak, J.M. Rickman, and C. Michaelsen. Evolution of grain structure in thin film reactions. *J. Elec. Mat.*, 26:1009–1020, 1997.

[85] K. Barmak, J.M. Rickman, C. Michaelsen, R.A. Ristau, J. Kim, G.A. Lucadamo, D.T. Carpenter, and W.S. Tong. Ex situ characterization of phase transformations and associated microstructures in polycrystalline thin films. *J. Vac. Sci. and Technol.*, 17:1950–1957, 1999.

[86] A. Schenkel, P. Wittwer, and J. Stubbe. Asymptotics of solutions in an A + B $\rightarrow$ C reaction-diffusion system. *Physica D: Nonlinear Phenomena*, 69:135–147, 1993.

[87] A.M. Turing. The chemical basis of morphogenesis. *Philos. Trans. R. Soc. Series B, Biological Sciences*, 237:37–72, 1952.

[88] C. McNamara, J.M. Rickman, and H.M. Chan. Kinetics and associated microstructure for reactive phase formation. *Acta Materialia*, 222:117456, 2022.

[89] C. McNamara, J.M. Rickman, H.M. Chan, and J. Zhang. Interacting fronts in a model of entropy-stabilized reactive phase formation. *Journal of Applied Physics*, 134:215105, 2023.

[90] M.M. Clark. *Transport Modeling for Environmental Engineers and Scientists*. John Wiley & Sons, 2009.

[91] L.G. Harrison. Influence of dislocations on diffusion kinetics in solids with particular reference to the alkali halides. *Trans. Faraday Soc.*, 57:1191–1199, 1961.

[92] R.T.P. Whipple. CXXXVIII. concentration contours in grain boundary diffusion. *Phil. Mag.*, 45:1225–1236, 1954.

[93] I. Kaur, Y. Mishin, and W. Gust. *Fundamentals of Grain and Interphase Boundary Diffusion*. John Wiley & Sons, 3rd edition, 1995.

[94] D.G. Duffy. *Green's Functions with Applications*. Chapman and Hall, 2nd edition, 2015.

[95] Y.A. Melnikov and M.Y. Melnikov. *Green's Functions: Construction and Applications*. DeGruyter, 2012.

[96] J. Tang, X. Geng, D. Li, Y. Shi, J. Tong, H. Xiao, and F. Peng. Machine learning-based microstructure prediction during laser sintering of alumina. *Sci. Rep.*, 11, 2021.

[97] W. Yan, J. Melville, V. Yadav, K. Everett, L. Yang, M.S. Kesler, A.R. Krause, M.R. Tonks, and J.B. Harley. A novel physics-regularized interpretable machine learning model for grain growth. *Materials & Design*, 222:111032, 2022.

[98] R. Liu, A. Kumar, Z. Chen, A. Agrawal, V. Sundararaghavan, and A. Choudhary. A predictive machine learning approach for microstructure optimization and materials design. *Sci. Rep.*, 6, 2015.

Appendix A

Code

```
(* Reaction-diffusion model: currently set for the lanes microstructure *)

Clear["Global`*"];
plt = 1; (* Set the amount of C needed to grow more C *)
numruns = 60; (* number of runs *)
numiter = 600;(* number of iterations *)
Numi = ( N[numiter]) + 1;
timelist = {};
productarray = {};

Do[
  (* Initialization of arrays *)
  profr = {}; (* Array for C: updaed after each iteration *)
  profa = {}; (* Array for A: updaed after each iteration *)
  profb = {}; (* Array for B: updaed after each iteration *)
  profilea = {}; (* Array for A: updaed after each run *)
  profileb = {}; (* Array for B: updaed after each run *)
  profilereac = {}; (* Array for C: updaed after each run *)
  Do[
    (* Initialize the microstructure *)
    blocksh = 14; (* Number of horizontal blocks *)
    blocksu = 10; (* Number of veritcal blocks *)
    sizeh = 10; (* Horizontal size of blocks *)
    sizeu = 10; (* Vertical size of blocks *)
    length = blocksh * sizeh; (* Overall length *)
    height = blocksu * sizeu; (* Overall height *)
    ncells = length * height; (* number of cells *)
    reacl = ConstantArray[0, ncells];
    reach = ConstantArray[0, ncells];

    (* Arrays for monitoring *)
    counterreac = Table[0, {i, 1, height}, {j, 1, length}];
    counterdiff = Table[0, {i, 1, height}, {j, 1, length}];
    totreacarray = Table[0, {i, 1, height}, {j, 1, length}];

    (* The number of atoms must be even *)
    numpatoma = 200; (* number of A atoms in a cell *)
    numpatomb = 200; (* number of B atoms in a cell *)

    nreactions = 1; (* number of reactions *)
    (* Diffusion rate is set at the end of the code *)
    nspecies = 2; (* Number of types of atoms *)
    ndirections = 4;
```

```
(* Number of possible directions for diffusion or reaction *)
reacratel = 0.0000;  (*  low reaction rate to be determined *)
reacrateh = 50;  (* high reaction rate to be determined *)
tau = 1.0; (* Tau to be determined *)

diffratio = 1; (* Ratio of db to da *)

(* Periodic boundary conditions. *)

pbcr[x_] := If[x < height, x + 1, 1]; (* Right *)
pbcl[x_] := If[x > 1, x - 1, height]; (* Left *)
pbcu[x_] := If[x > 1, x - 1, length]; (* Up *)
pbcd[x_] := If[x < length, x + 1, 1]; (* Down *)


(* Initialize the location of atoms *)

xcell = {}; (* The microstructure *)
tempx = {};

(* Set the location of A and B *)
xcell = Table[If[EvenQ[Ceiling[i, 20] / 20],
   {numpatoma, 0, 0}, {0, numpatomb, 0}], {i, 1, height}, {j, 1, length}];

(* Set the location of C atoms *)
Do[
 xcell = ReplacePart[xcell, {i1, 1} → {0, 0, 10}]
 , {i1, 1, height}];

startsys = xcell;

(* Set another series of tracking tables *)
AppendTo[profr, Table[xcell⟦i⟧⟦j⟧⟦3⟧, {j, 1, length}, {i, 1, height}]];
AppendTo[profa, Table[xcell⟦i⟧⟦j⟧⟦1⟧, {j, 1, length}, {i, 1, height}]];
AppendTo[profb, Table[xcell⟦i⟧⟦j⟧⟦2⟧, {j, 1, length}, {i, 1, height}]];

xbegin = xcell;
Do[

 tempx = xcell;

 (* Initialize time to zero *)
 time = 0;
```

```
position1 = 1;
position2 = 1;

(* Random chocie if reaction or diffusion is first *)
loop = RandomInteger[{1, 2}];
If[loop == 2, Goto[tagb]];

(* Determine the current reaction rate based on the atom count *)

Label[taga];
(* Reaction *)
Do[
 Do[
   (* Random choice of cell *)
   k = RandomSample[RandomSample[Range[height]], 1][[1]];
    RandomInteger[{5, 5}];
   j = RandomSample[RandomSample[Range[length]], 1][[1]];
    RandomInteger[{5, 5}];

   (* Increase count for reaction event: debugging purposes *)
   counterreac[[k]][[j]] = counterreac[[k]][[j]] + 1;

   (* Make changes to the current cell and
    the neighboring cell according to the poisson value *)
   xpick = 0;
   ypick = 0;
   xpick = xcell[[k]][[j]][[1]]; (* a atoms *)
   ypick = xcell[[k]][[j]][[2]]; (* b atoms *)

   (* Calculate amount of C in the surrounding cells *)
   lreac = xcell[[pbcl[k]]][[j]][[3]];
   rreac = xcell[[pbcr[k]]][[j]][[3]];
   ureac = xcell[[k]][[pbcu[j]]][[3]];
   dreac = xcell[[k]][[pbcd[j]]][[3]];

   (* Calcualte amount of C for the plating *)
   totreac = IntegerPart[lreac] +
     IntegerPart[rreac] + IntegerPart[ureac] + IntegerPart[dreac];

   totreacarray[[k, j]] = totreac;

   (* Drfine amount the system will react *)
   prate = 0.0;
   If[ totreac ≥ plt, prate = RandomVariate[PoissonDistribution[
```

```
        tau * reacrateh * (xpick / numpatoma) * (ypick / numpatomb) + 0.000001]];
     prate = Round[prate]];

     (* Check reaction rate is possible *)
    If[xpick == 0, prate = 0];
    If[ypick == 0, prate = 0];
    If[xpick < ypick,
     If[xpick < prate, prate = xpick],
     If[ypick < prate, prate = ypick]];

    (* Make changes to the system *)
    xcell⟦k⟧⟦j⟧⟦1⟧ = xcell⟦k⟧⟦j⟧⟦1⟧ - prate;
    xcell⟦k⟧⟦j⟧⟦2⟧ = xcell⟦k⟧⟦j⟧⟦2⟧ - prate;
    xcell⟦k⟧⟦j⟧⟦3⟧ = xcell⟦k⟧⟦j⟧⟦3⟧ + prate;

    (* Increase counts *)
    , {e, 1, 1}] ;
  , {q, 1, ncells}];


If[loop == 2, Goto[tagc]];

Label[tagb];

(* Diffusion *)
Do[
 Do[
   Do[
     (* Random pick of A or B to diffuse *)
     i = RandomInteger[{1, nspecies}];
      RandomInteger[{5, 5}];
     (* Random chocie of location *)
      k = RandomSample[RandomSample[Range[height]], 1]⟦1⟧;
      RandomInteger[{5, 5}];
     j = RandomSample[RandomSample[Range[length]], 1]⟦1⟧;

     (* Diffusion event counter: debugging purposes *)
     counterdiff⟦k⟧⟦j⟧ = counterdiff⟦k⟧⟦j⟧ + 1;

     (* Random chocie for diffusion direction *)
     l = RandomChoice[{1, 2, 3, 4}];

     td  = tau * diffrate;
```

```
      (* Check for atoms in the
       diffusing cell and adjust the amount to be diffused *)
      xpick = xcell⟦k⟧⟦j⟧⟦i⟧;
      If[xpick < 0, Print[xpick]; Print[iter]; Goto[tagd];];
      (* For debugging purpose *)
      If[xpick > 0, prate = RandomVariate[TruncatedDistribution[{-0.1, xpick},
          PoissonDistribution[tau * diffrate]]], prate = 0];

      prate = Round[prate];

      (* Define the neighbor cell according to the random variable *)
      If[l == 1, neighcellx = pbcl[k]; neighcelly = j];
      If[l == 2, neighcellx = pbcr[k]; neighcelly = j];
      If[l == 3, neighcelly = pbcu[j]; neighcellx = k];
      If[l == 4, neighcelly = pbcd[j]; neighcellx = k];

      (* Update the tables with the new values *)
      If[neighcellx < 1, Print["problem x"]];
      If[neighcelly < 1, Print["problem y"]];
      If[xpick > 0, xcell⟦k⟧⟦j⟧⟦i⟧ = xcell⟦k⟧⟦j⟧⟦i⟧ - prate;
       xcell⟦neighcellx⟧⟦neighcelly⟧⟦i⟧ =
        xcell⟦neighcellx⟧⟦neighcelly⟧⟦i⟧ + prate;];



      position2 = position2 + 1;

      , {ii, 1, nspecies}];
    , {e, 1, 1}] ;
  , {kk, 1, ncells}];

If[loop == 2, Goto[taga]];

Label[tagc];

(* Update time *)
time = time + tau;

(* Print iterations at set intervals: debugging and monitering *)
If[Mod[iter, 100] == 0, Print["No. of iterations: ", iter]];

(* Update tables for the iteration *)
AppendTo[profr, Table[xcell⟦j⟧⟦i⟧⟦3⟧, {i, 1, length}, {j, 1, height}]];
AppendTo[profa, Table[xcell⟦j⟧⟦i⟧⟦1⟧, {i, 1, length}, {j, 1, height}]];
```

```
   AppendTo[profb, Table[xcell⟦j⟧⟦i⟧⟦2⟧, {i, 1, length}, {j, 1, height}]];

   (* End of iteration *)
   , {iter, 1, numiter}];

  (* Update tables for the run *)
  AppendTo[profilea, Table[xcell⟦i⟧⟦j⟧⟦1⟧, {j, 1, length}, {i, 1, height}]];
  AppendTo[profileb, Table[xcell⟦i⟧⟦j⟧⟦2⟧, {j, 1, length}, {i, 1, height}]];
  AppendTo[profilereac, Table[xcell⟦i⟧⟦j⟧⟦3⟧, {j, 1, length}, {i, 1, height}]];
  AppendTo[productarray,
   Table[xcell⟦i⟧⟦j⟧⟦1⟧ * xcell⟦i⟧⟦j⟧⟦2⟧, {j, 1, length}, {i, 1, height}]];
  AppendTo[timelist, time];

  (* Print runs at set intervals: debugging and monitering *)
  If[Mod[nruns, 1] == 0, Print["No. of runs: ", nruns]],

  (* End of run *)
  {nruns, 1, numruns}] ×
 Label[tagd];

(* Create empty arrays *)
ploa = {};
plob = {};
profile = {};

(* Calculate and save the data for an average of all runs *)
Do[
 AppendTo[ploa, Sum[profa⟦i⟧, {i, j, N[(numruns * Numi)], Numi}] / numruns];
 AppendTo[plob, Sum[profb⟦i⟧, {i, j, N[(numruns * Numi)], Numi}] / numruns];
 , {j, 1, Numi}];
Do[
 AppendTo[profile, Sum[profr⟦i⟧, {i, j, N[(numruns * Numi)], Numi}] / numruns];
 , {j, 1, Numi}];

(* Set the name and location where the data will be saved *)
namea = "/Users/connor/Documents/Research/Concentration/LCDR 102/par50d" <>
  ToString[diffrate] <> ".mx";
nameb = "/Users/connor/Documents/Research/Concentration/LCDR 102/pbr50d" <>
  ToString[diffrate] <> ".mx";
namec = "/Users/connor/Documents/Research/Concentration/LCDR 102/pcr50d" <>
  ToString[diffrate] <> ".mx";

(* Export the data as .mx files *)
Export[namea, ploa];
```

```
Export[nameb, plob];
Export[namec, profile];

(* Set the diffusion rate here *)
, {diffrate, 10, 10}];
```

Vita

Connor P. McNamara was born on April 9^{th}, 1991 in Birmingham, Alabama to Frank and Maryann McNamara. He grew up in Somers, Connecticut. Connor graduated from Lafayette College in 2013 with a Bachelor of Science in Mechanical Engineering. Looking to advance his career prospects, he then graduated from Drexel University in 2016 with a Masters of Science in Mechanical Engineering. He worked for Belcan as a Structural Engineer doing simulation work for Pratt and Whitney and United Technologies Aerospace Systems. While working there, Connor realized he was more interested in the materials aspect of the work he witnessed being done, but still wanted to focus on simulation and modeling. In 2019, he joined Professor Helen Chan's group as her then lone PhD student. Under Professors Chan and Jeffrey Rickman, Connor researched the kinetic modeling of solid state synthesis, using the formation of $CoTi_2O_5$ from $CoTiO_3$ and TiO_2 as a laboratory counterpoint.